

Assessment of smoke plume height products derived from multisource satellite observations using lidar-derived height metrics for wildfires in the western US

Jingting Huang^{1,*}, S. Marcela Loría-Salazar², Min Deng³, Jaehwa Lee^{4,5}, Heather A. Holmes¹

5 ¹ Department of Chemical Engineering, University of Utah, Salt Lake City, 84112 UT, USA

² School of Meteorology, University of Oklahoma, Norman, 73072 OK, USA

³ Environmental and Climate Sciences Department, Brookhaven National Laboratory, Upton, 11973 NY, USA

⁴ Earth System Science Interdisciplinary Center, University of Maryland, College Park, 20740 MD, USA

⁵ NASA Goddard Space Flight Center, Greenbelt, 20771 MD, USA

10

Correspondence to: Jingting Huang (jingting.huang@utah.edu)

Abstract. As wildfires intensify and fire seasons lengthen across the western U.S., the development of models that can predict smoke plume concentrations and track wildfire-induced air pollution exposures has become critical. Wildfire smoke plume height is a key indicator of the vertical placement of plume mass emitted from wildfire-related aerosol sources in climate and air quality models. With advancements in Earth observation (EO) satellites, spaceborne products for aerosol layer height or plume injection height have recently emerged with increased global-scale spatiotemporal resolution. However, to evaluate column radiative effects and refine satellite algorithms, vertical profiles of regionally representative aerosol properties from wildfires need to be measured directly. In this study, we conducted the first comprehensive evaluation of four passive satellite remote sensing techniques specifically designed for retrieving plume height. We compared these satellite products with the airborne Wyoming Cloud Lidar (WCL) measurements during the 2018 Biomass Burning Flux Measurements of Trace Gases and Aerosols (BB-FLUX) field campaign in the western U.S. Two definitions, namely “plume top” and “extinction-weighted mean plume height”, were used to derive representative heights of wildfire smoke plumes, based on the WCL-derived vertical aerosol extinction coefficient profiles. Using these two definitions, we performed a comparative analysis of multisource satellite-derived plume height products for wildfire smoke. We provide a discussion related to which satellite product is most appropriate for determining plume height characteristics near a fire-event or estimating downwind plume rise equivalent height, under multiple aerosol loadings. Our findings highlight the importance of understanding the sensitivity of different passive remote sensing techniques on space-based wildfire smoke plume height observations, in order to resolve ambiguity surrounding the concept of “effective smoke plume height”. As additional aerosol-observing satellites are planned in the coming years, our results will inform future remote sensing missions and EO satellite algorithm development. This bridges the gap between satellite observations and plume rise modeling to further investigate the vertical distribution of wildfire smoke aerosols.

1 Introduction

Characterizing the vertical extent of wildfire smoke aerosols near active fire hotspots, also known as plume injection height (PIH) or smoke aerosol layer height (ALH), is a critical task in simulating the long-range transport of wildfire smoke. From a physical perspective, the initial PIH at a fire can be described as the height where the relatively stable vertical atmospheric layer is located, causing the smoke plume to accumulate, and where the updrafts generated by the buoyancy above the fire terminate (Kahn et al., 2007; Labonne et al., 2007; Paugam et al., 2015). PIH is commonly viewed as the vertical height to which a buoyant plume core can lift the polluted air mass before the smoke plume begins to bend over horizontally (Raffuse et al., 2012). Often plume heights

near or downwind of active fire areas are treated as equivalent to PIH values. Wildfire smoke plumes move horizontally in single layers through the atmosphere, but some may become stratified into multiple, discrete layers (Mardi et al., 2018; Deng et al., 2022b). However, it is impossible to distinguish aerosol layering at multiple heights without vertically resolved smoke aerosol profiles. Consequently, a single height value is often applied and obtained from physics-based numerical models or passive remote sensing retrievals. Regardless of whether the vertical structure of wildfire smoke aerosols is homogenous or heterogenous, a columnar plume height retrieved from satellites is considered a representative ALH. This study focuses on the smoke-specific plumes from wildfires in the western United States (WUS); therefore, we will use smoke plume height (*SPH*) to denote this.

Wildfire *SPH* observed from space has advanced in spatiotemporal resolution since the 2000s (Kahn et al., 2007; Ichoku et al., 2012; Lyapustin et al., 2019; Kahn, 2020). Passive satellite sensors are used to map global wildfire *SPH* distribution, spanning a range of recently developed techniques and retrieval algorithms. It is important to note that each method to obtain satellite *SPH* retrievals utilizes a distinct remote sensing technique, resulting in inconsistent definitions of *SPH*. To shed light on their differences, a brief overview of these methods is provided to demonstrate why they yield differing plume height interpretations.

The photogrammetric stereo capability of the Multi-Angle Imaging SpectroRadiometer (MISR) aboard the National Aeronautics and Space Administration (NASA) Earth Observing System's Terra spacecraft (Diner et al., 1998), combined with the MISR Interactive Explorer (MINX) tool (Nelson et al., 2008, 2013), provides "wind-corrected" *SPH* values of elevated smoke aerosols. This approach takes into account feature displacements caused by the plume movement and the stereo parallax shift among different camera views. Another approach to retrieve *SPH* takes advantage of the altitude dependence of absorption spectroscopic characteristics of molecular oxygen (O_2) in the A band at 759–771 nm or the B band at 686–695 nm or the O_2 – O_2 spectral band at 477 nm. This approach has been successfully applied to a number of passive satellite-supported instruments, including but not limited to POLDER/PARASOL (the POLarization and Directionality of the Earth's Reflectance mounted on the Polarization and Anisotropy of Reflectances for Atmospheric Sciences coupled with Observations from a Lidar platform, Dubuisson et al., 2009), MERIS/ENVISAT (the MEdium Resolution Imaging Spectrometer installed on the Environmental Satellite, Duforêt et al., 2007; Dubuisson et al., 2009), SCIAMACHY/ENVISAT (the SCanning Imaging Absorption SpectroMeter for Atmospheric CHartographY on board the Environmental Satellite, Corradini and Cervino, 2006; Sanghavi et al., 2012), GOME-2/MetOp (the Global Ozone Monitoring Experiment–2 flying on the Meteorological Operational series of satellites, Sanders et al., 2015; Nanda et al., 2018a; Michailidis et al., 2021), OMI/Aura (the Ozone Monitoring Instrument aboard the Aura spacecraft, Chimot et al., 2017, 2018), EPIC/DSCOVER (the Earth Polychromatic Imaging Camera loaded on the Deep Space Climate Observatory, Xu et al., 2019; Lu et al., 2021) and TROPOMI/S-5 P (the TROPospheric Monitoring Instrument carried on the Copernicus Sentinel-5 Precursor mission, Griffin et al., 2020; Nanda et al., 2020; Chen et al., 2021). Other approaches utilize the ultraviolet (UV; 340–380 nm) or thermal infrared (TIR; 11 μ m) bands, which are sensitive to the vertical distribution of absorbing aerosols (e.g., smoke and mineral dust) or absorption by gases released from fires (together with smoke aerosols), respectively. Using bands included in wide-swath passive sensors means that these approaches can provide *SPH* globally. Based on the sensitivity of backward UV radiance to the height of absorbing aerosols (e.g., dust and smoke) in a Rayleigh scattering atmosphere (Hsu et al., 1996; Torres et al., 1998; Hsu et al., 1999), previous studies proposed an algorithm called the Aerosol Single-scattering albedo and Height Estimation (ASHE) that jointly retrieves ALH and single scattering albedo (SSA) using UV-aerosol index (UVAI), aerosol optical depth (AOD), and spaceborne lidar backscatter profile from multi-sensor measurements (Jeong and Hsu, 2008; Lee et al., 2015, 2016). In a subsequent study, Lee et al. (2020) revised the ASHE algorithm to function without the lidar backscatter profile.

Lyapustin et al. (2019) and Cheeseman et al. (2020) introduced the brightness temperature contrast approach that uses the Moderate Resolution Imaging Spectroradiometer (MODIS) TIR band (11 μ m) for smoke plume identification and characterization. Using

this technique, daily *SPH* values are retrieved on a global sinusoidal grid as part of the Multi-Angle Implementation of Atmospheric Corrections (MAIAC) atmospheric product MCD19A2.

Passive satellites provide widespread coverage on a regular basis, all while incurring minimal recurring costs and posing no risks to observers. Yet, dense smoke plumes, cloud cover, or scan gaps between adjoining orbits of sun-synchronous polar satellites can result in unsuccessful retrievals (Lyapustin et al., 2008). As a complement to these passive retrievals, active spaceborne lidars like CALIOP/CALIPSO (the Cloud-Aerosol Lidar with Orthogonal Polarization aboard the Cloud-Aerosol Lidar and Infrared Pathfinder Satellite Observation satellite, Winker et al., 2009) and CATS/ISS (the Cloud-Aerosol Transport System installed on the International Space Station, McGill et al., 2015) offer high-resolution vertical profiles of aerosol optical signals. While these spaceborne lidars enhance the detection of thin smoke layers, they are bound by a narrow, pencil-like swath providing limited spatial coverage, see Figure 9 in Loria-Salazar et al. (2021). Another limitation of remote sensing instruments on polar-orbiting satellites is that they do not resolve the diurnal variation of wildfire activity.

Endeavors to investigate fire behavior and their associated air quality (AQ) impacts have predominantly relied on the use of field data and satellite-based retrievals. Passive and active remote sensing techniques are complementary because of their different observational methods. The deliberate collocation of them provides synergistic insights into missing pieces of fire information that may not be attainable by either type of technique in isolation (Liu et al., 2019a; Sicard et al., 2019). Unfortunately, in the Intermountain West region of the U.S., there remains a lack of detailed vertical profiles of aerosol optical properties, despite recent field experiments such as Fire Influence on Regional to Global Environments and Air Quality (FIREX-AQ), Western wildfire Experiment for Cloud chemistry, Aerosol absorption and Nitrogen (WE-CAN), Biomass Burning Flux Measurements of Trace Gases and Aerosols (BB-FLUX), and Fire and Smoke Model Evaluation Experiment (FASMEE). Furthermore, to date, there is no universally accepted methodology for directly deriving *SPH* from aerosol extinction or backscatter vertical profiles due to the ambiguous use and definition of the term “effective *SPH*” (Xu et al., 2017). This poses a challenge, particularly when one wants to compare columnar *SPH* values from passive remote sensors with retrieved three-dimensional (3D) distribution of smoke aerosol vertical structure from active remote sensors.

The primary objective of this study is to address the central research question: which *SPH* definition corresponds to the most physically relevant plume height for a specific satellite *SPH* retrieval algorithm? We introduce two *SPH* definitions using vertical profiles of smoke aerosol from airborne lidar data. We then quantify the sensitivity of four passive remote sensing techniques to columnar *SPH* observations with respect to these two definitions, accounting for the effects of local meteorology, distance from the active fire source, and smoke aerosol loading. Meanwhile, we explore an optimal collocation strategy to compare satellite retrievals with lidar measurements, considering instrument discrepancies in observing *SPH* experimentally. To the best of our knowledge, we present the first comprehensive assessment of multiple satellite-derived *SPH* products compared with aircraft lidar data. It is important to note here that there were no coincident satellite-based lidar overpasses for our field campaign data; therefore, they are not included in our results. This omission underscores the difficulties in directly comparing spaceborne lidar products with data from aircraft campaigns. The results of our study clarify the meaning of “effective *SPH*” in the remote sensing and modeling communities, filling a critical gap in uniform plume height comparisons. Our findings also meet the urgent need for a suite of remotely sensed datasets to evaluate the performance of present and future dynamic smoke plume models and smoke modeling frameworks, or to provide inputs to these models that improve the *SPH* characterization required to model the downwind pollutant transport.

2 Measures of wildfire *SPH*

115 2.1 Satellite-based wildfire *SPH*

The following four space-based wildfire *SPH* retrievals will be discussed in our study: (1) MODIS aerosol product using the MAIAC algorithm (MODIS/MAIAC); (2) MISR-based global *SPH* database that can be accessed via the MISR Enhanced Research and Lookup Interface (MISR/MERLIN); (3) Visible Infrared Imaging Radiometer Suite (VIIRS) aerosol product using the ASHE algorithm (VIIRS/ASHE); (4) TROPOMI-based ALH product (TROPOMI/ALH). Here, the *SPH* products from the different
 120 instruments retrieved with different methods are named using the passive sensor name and the corresponding retrieval algorithm or dataset name. **Table 1** provides further information about these passively remote-sensed *SPH* products.

Table 1: Summary of multisource satellite-derived plume height products.

| Data Set/Version | Availability | Resolution | Instrument/Satellite | Retrieval Method | References |
|--|--|--|-------------------------|---------------------------------|-------------------------|
| MAIAC-derived injection height products/collection 6.1 | February 1, 2000 to present | <i>horizontal</i> : 1 km × 1 km | MODIS/Terra or Aqua | Brightness temperature contrast | Lyapustin et al. (2019) |
| | | <i>temporal</i> : 16-day repeating cycle; one-to-two-day global coverage | | | |
| MERLIN interface for MISR plume height project/version 2 | 2008–2011 as well as the summers (June, July, August) of 2017 and 2018 | <i>horizontal</i> : 1.1 km × 1.1 km | MISR/Terra | Multi-angle imaging | Kahn et al. (2007) |
| | | <i>temporal</i> : 16-day repeating cycle; 9-day global coverage | | | |
| ASHE-derived ALH products/research | August of 2013–2018 | <i>horizontal</i> : 6 km × 6 km | VIIRS/SNPP ^a | Ultraviolet radiometry | Lee et al. (2020) |
| | | <i>temporal</i> : 16-day repeating cycle; daily global coverage | | | |
| TROPOMI level-2 ALH/version 1 | April 30, 2018 to July 1, 2021 | <i>horizontal</i> : 3.5 km × 7 km (across x along track) from April 30, 2018 to August 6, 2019; 3.5 km × 5.5 km since August 6, 2019 | TROPOMI/S-5 P | Oxygen absorption | Sanders et al. (2012) |
| | | <i>temporal</i> : 16-day repeating cycle; near-daily global coverage | | | |

^a Data from VIIRS sensors on other satellite platforms were unavailable for this study.

2.1.1 MODIS/MAIAC

125 MODIS sensors are located on the Terra (morning sensor, 10:30 AM local solar time crossing the equator) and Aqua (afternoon sensor, 1:30 PM local solar time crossing the equator) satellite platforms and operate in the TIR spectrum to detect active fires (Salomonson et al., 2002). This twin-MODIS design covers most regions near the equator with at least four observations per day. The number of observations increases as one approaches the poles due to overlapping orbits. The MAIAC algorithm uses MODIS data to obtain near-fire-source aerosol injection height, known as the MCD19A2 dataset with high resolution (1 km).

130 By assuming a fixed lapse rate, the MAIAC PIH algorithm utilizes negative thermal contrast at 11 μm between smoke and sufficient
neighboring smoke-free pixels and converts the colder brightness temperature into *SPH* estimates (Lyapustin et al., 2019;
Cheeseman et al., 2020). The valid range for the MAIAC-based *SPH* is up to 10 km. However, the *SPH* calculation struggles with
large smoke areas and small fires emitting low levels of absorbing gases, meaning it requires a high enough plume opacity (AOD
at 470 nm ≥ 0.8) to obtain a useful signal. When compared to other *SPH* datasets such as MISR and CALIOP, MAIAC tends to
135 significantly underestimate the height of smoke plumes, particularly for transporting dilute smoke downwind of the fire (Lyapustin
et al., 2019). In spite of these limitations, the MAIAC algorithm provides valuable information within approximately 75–150 km
of the identified thermal hotspots, i.e., fire (Loría-Salazar et al., 2021).

2.1.2 MISR/MERLIN

With its nine fixed push-broom cameras, MISR aboard NASA's Terra satellite captures images from nine different angles and four
140 spectral bands, allowing for studies of wildfire and aerosol distributions using the stereoscopic technique, unaffected by bright
surfaces (Moroney et al., 2002; Muller et al., 2002). The wealth of data collected by the MISR instrument over two decades offers
valuable insights into the global climatology of fire in the environment, across geographic regions, biomes, and seasons (Val Martin
et al., 2018; Gonzalez-Alonso et al., 2019). The publicly available database built using manually postprocessed MISR products
has been used to evaluate plume rise models (e.g., Ke et al., 2021) and other satellite-derived datasets (e.g., Lyapustin et al., 2019;
145 Griffin et al., 2020). Recently, an interactive visualization tool called MERLIN was developed to facilitate the exploration and
accessibility of over 70,000 records of global wildfire plume height retrievals (Boone et al., 2018; Nastan et al., 2022).

MISR's global *SPH* mapping, with a 250–500 m vertical resolution, complements aerosol height curtains obtained from spaceborne
lidar systems (Kahn et al., 2007, 2008; Val Martin et al., 2018). However, Tosca et al. (2011) found that stereo-derived *SPH* from
MISR was significantly lower than the top altitude observed by CALIOP for the 2006 Indonesian fires. Nevertheless, important
150 lessons can be drawn from the underestimated *SPH* values in the MISR product as follows: (1) the overpass time of MISR in the
morning precedes the daytime peak in fire activity, typically in late afternoons when temperatures are highest and relative humidity
is lowest; (2) very few coincident overpasses exist over fires during a short time of interest due to the narrow MISR swath, which
allows global coverage only approximately once per week. Additionally, the revisit period of MISR for a specific geographical
spot varies from 2 to 9 days, depending on the latitude (Kahn et al., 2007); (3) MISR automated stereoscopic image's dependence
155 on optically distinct plume-like features for accurate height estimation can introduce bias, mainly when dealing with thin smoke
or smoke downwind of the active fire source with less defined boundaries (Nelson et al., 2013). However, blue-band data at 1.1
km horizontal cell size is considered a better choice for capturing the higher injection heights associated with fine smoke aerosols
than the corresponding red-band retrievals at the spatial resolution of 275 m (Nelson et al., 2013). In this study, we extracted blue-
band, wind-corrected heights with "good" quality flags downloaded from MERLIN. This preference is due to the blue band's
160 $(446.4 \pm 41.9 \text{ nm})$ sensitivity to thinner aerosol layers, enabling the detection of aerosol features at higher altitudes.

2.1.3 VIIRS/ASHE

The launch of operational VIIRS sensors has been planned for the Joint Polar Satellite System (JPSS) series since 2011, in
anticipation of the post-MODIS era (Cao et al., 2013a, 2013b; Goldberg et al., 2013; Wolfe et al., 2013; Wang and Cao, 2019).
VIIRS currently flies on three polar-orbiting satellites: Suomi National Polar-orbiting Partnership (SNPP), National Oceanic and
165 Atmospheric Administration-20 (NOAA-20) and NOAA-21 satellites. This study uses data from SNPP VIIRS. The VIIRS
instrument has a wide swath of 3,040 km and can observe the entire Earth twice a day — once during the day and once during the

night. There are some overlaps between consecutive swaths, which means that mid-latitudes will experience up to 4 looks per day (Wolfe et al. 2013). Even though the SNPP VIIRS data has enhanced radiometric measurement quality, a broad spectral range, and a fine spatial resolution (Csiszar et al., 2014; Schroeder et al., 2014), the limited temporal information may curtail its efficacy for delineating fire perimeters and assessing fire spread, especially during short fire durations (Cardil et al., 2019).

The research version of the ASHE algorithm (transition to operational processing is underway at the time of writing) provides the plume height of UV-absorbing aerosols like smoke and dust over broad areas, including both near-source and transported plumes (Loría-Salazar et al., 2021). Initially, it leveraged AOD and Ångström Extinction Exponent (AEE) from the MODIS or VIIRS aerosol product in its retrieval process, as well as ALH along the CALIOP track as a constraint (Jeong and Hsu, 2008; Lee et al., 2015). By assuming spatially invariant SSA retrieved along the CALIOP track over a MODIS/VIIRS granule, the height retrieval can be extended beyond the narrow CALIOP track, thereby improving spatiotemporal coverage. This study makes use of a release candidate of ASHE, that does not use the CALIOP constraints and leverages the synergy between VIIRS and Ozone Mapping and Profiler Suite - Nadir Mapper (OMPS-NM) for UV measurements (Lee et al., 2020). To further improve its performance, a systematic optimization of the smoke optical models used in the algorithm was carried out by iteratively comparing the retrieved ALH and SSA with those from CALIOP and ground-based measurements offline until satisfactory similarity was found between the results (e.g., Jeong et al., 2022). Its application is limited to UV-absorbing aerosols with moderate to thick optical depths (AOD at 550 nm > 0.5–1.0), rendering it ineffective for aerosols with lower optical depths. Preliminary evaluation indicates the ASHE-retrieved *SPH* has an uncertainty of 1–1.2km (or 30–40% for *SPH* of 3 km) for heavy aerosol loading cases (AOD > 1) (Lee et al., 2016, 2020). The uncertainty is dependent on errors in retrieved AOD, assumed aerosol optical model, and surface reflectance, and generally decreases with increasing AOD. It should be noted that OMPS-NM aboard SNPP has a relatively coarse spatial resolution of $\sim 50 \times 50 \text{ km}^2$ near nadir ($\sim 200 \times 100 \text{ km}^2$ near the edge of the across-track scan), indicating that it has limitations for small-scale (subpixel) smoke plumes. Although there are multiple VIIRS instruments, the ASHE product is currently only available for SNPP VIIRS. It is anticipated that this retrieval algorithm will be implemented for other VIIRS instruments in the future.

2.1.4 TROPOMI/ALH

The TROPOMI instrument is the single payload on board of the European Space Agency (ESA) S-5 P satellite mission, planned for 2017–2024. TROPOMI is a spectrometer that monitors key atmospheric constituents and aerosol/cloud properties by observing reflected sunlight across the spectral bands in the UV, the visible (270–500 nm), the near-TIR (675–775 nm), and the shortwave TIR (2305–2385 nm). Compared to its predecessors (OMI and SCIAMACHY), TROPOMI provides high spatially resolved information and is capable of daily global coverage and near real-time data, which enables regular monitoring and rapid assessment of changes in the Earth’s atmosphere (Veefkind et al., 2012).

By analyzing the spectral signature of light that is absorbed by O₂ in the A band in the near-TIR wavelength range between 759 and 770 nm, the TROPOMI ALH algorithm estimates the height of aerosol plumes in the atmosphere (Sanders et al., 2012; Nanda et al., 2019). It has shown to be effective in retrieving high plumes up to 8 km in height above ground level (AGL), with reduced uncertainties for thicker and lower plumes between 1 and 4.5 km in height AGL (Griffin et al., 2020), as well as for dark surfaces (Nanda et al., 2018b). However, it was found to be biased low compared with other *SPH* datasets such as MISR and CALIOP, most likely due to its tendency to return an intermediate plume height when multiple aerosol layers are present (Griffin et al., 2020; Nanda et al., 2020). In addition, Nanda et al. (2020) shows that cloud contamination has an impact on the TROPOMI/ALH product since it is unable to distinguish between cloud and aerosol signals from the measured radiances. In this study, we only used data having a quality assurance value larger than 0.5 to filter and remove the predominately cloudy scenes or retrievals with geolocation

2.2 Airborne lidar measurements

The 2018 BB-FLUX field campaign deployed the upward-pointing Wyoming Cloud Lidar (WCL) on the University of Wyoming King Air (UWKA) research aircraft that sampled smoke plumes from more than 20 wildfires during 35 flights over the WUS. The airborne WCL measurements of attenuated backscattering coefficient and lidar depolarization ratio were calibrated on a per-flight basis. The vertical aerosol extinction profiles (units: km^{-1}) were retrieved with Fernald's method assuming a constant lidar ratio of 60 and evaluated with in situ measurements (see Deng et al., 2022a for details). **Table 2** lists nine wildfire cases, including locations, start and containment dates, and acres burned (Geospatial Multi-Agency Coordination Group, 2019). It also summarizes eleven flight missions from August 2018, selected for the number of collocated pairs between valid lidar transects and satellite overpasses, with the flight trajectories illustrated in **Fig. 1**. The chosen flights are limited to smoke plumes that could be attributed to a specific wildfire. Other flights during the campaign were excluded from this study because they target prescribed fires, small wildfires, clouds, and aged smoke plumes. Small fires were not included, in part, because of the expected large uncertainties in satellite retrievals of the relatively low *SPH* values (ranging from hundreds of meters for prescribed fires to thousands of meters for small fires). Large errors for smoke aerosol layers within the boundary layer arise from a mismatch between the coarse spatial resolution of satellite pixels and the fine-scale smoke plume variability inherent in wildfire activity (Geddes and Boesch, 2015).

We re-gridded valid WCL two-dimensional (2D) transects at a vertical resolution of 3 m and an along-track horizontal resolution of about 1.1 km to calculate *SPH* and columnar AOD throughout the atmosphere. Compared to satellite observations, the re-gridded WCL measurements have a much smaller field of view in the cross-track direction, therefore the WCL can show much finer spatial variations in smoke. Moreover, it should be noted that the WCL can be fully attenuated in dense smoke and unable to detect the actual *SPH*, and the aircraft might fly above the plume bottom, so the upward-looking WCL only samples partial AOD of the aerosol vertical profile, which fundamentally differs from the AOD derived from satellite retrievals.

Table 2: Summary of nine wildfire cases with its general information and the corresponding eleven flight missions from August 2018. A flight name is denoted by its date '+ a' because the flight occurred in the morning; otherwise, it is denoted by its date '+ b' if it occurred in the afternoon. Note that the average distance between the aircraft and the active fire source was estimated using the geodesic distance from the fire center to the reconstructed lidar vertical cross-section.

| Wildfire Name | Active Fire Location (Latitude, Longitude) | Start Date | Approximate Containment Date | Approximate Burned Area (acres) | Flight Date (UTC) | Flight Name | Aircraft Sampling Distance from Active Fire Source (km) | Nth Day After Fire Start Date |
|-----------------------|--|--------------|------------------------------|---------------------------------|-------------------|--------------|---|-------------------------------|
| Sharps Fire, ID | 43.467°N, 114.145°W | Jul 29, 2018 | Aug 12, 2018 | 64, 812 | 2018/08/03 | 0803a | 18.88 | 6 |
| | | | | | 2018/08/04 | 0804b | 46.50 | 7 |
| Rabbit Foot Fire, ID | 44.856°N, 114.307°W | Aug 2, 2018 | Sep 19, 2018 | 36, 031 | 2018/08/08 | 0808b | 21.86 | 7 |
| | | | | | 2018/08/12 | 0812a | 32.80 | 11 |
| Watson Creek Fire, OR | 42.653°N, 120.818°W | Aug 15, 2018 | Sep 9, 2018 | 59, 067 | 2018/08/19 | 0819a, 0819b | a: 5.26/b: 22.61 | 5 |

| | | | | | | | | |
|---------------------------------|------------------------|--------------|--------------|----------|------------|-----------------|-----------------|----|
| | | | | | 2018/08/24 | 0824a | 41.75 | 10 |
| | | | | | 2018/08/25 | 0825a | 13.17 | 11 |
| Sheep Creek Fire, NV | 40.773°N, 116.842°W | Aug 18, 2018 | Aug 23, 2018 | 59, 789 | 2018/08/20 | 0820a, 0820b | a: 1.70/b: 1.48 | 3 |
| South Sugarloaf Fire, NV | 41.812°N, 116.324°W | Aug 17, 2018 | Sep 3, 2018 | 233, 608 | 2018/08/23 | 0823a | 51.44 | 7 |

230

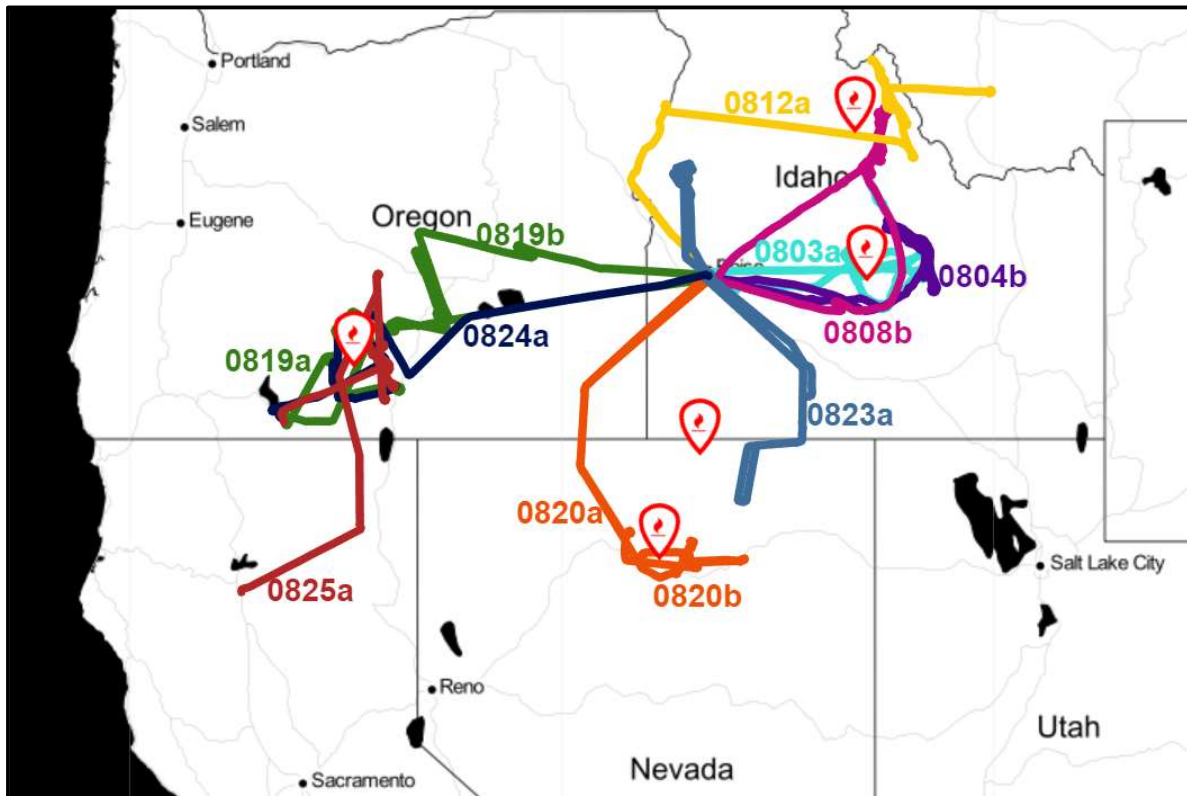


Figure 1: Color-coded eleven UWKA flight trajectories during the 2018 August BB-FLUX project, each of which is associated with one of nine wildfire cases denoted by fire icons.

3 Methods

235 3.1 Definitions of wildfire *SPH* estimates

The extinction coefficient is a key parameter for the fundamental radiative transfer calculations of wildfire smoke aerosols from the surface to the top of the atmosphere (TOA) (e.g., Ansmann et al., 2018; Solomon et al., 2022) and can be related to the particle mass (or volume) concentration (e.g., Mamouri and Ansmann, 2016; Toth et al., 2019; Ansmann et al., 2021). In previous studies, the aerosol extinction coefficient has been one of the most frequently observed and reported aerosol optical properties for

240 characterizing the vertical structure of the atmosphere and developing a height retrieval algorithm (Gordon, 1997; Dubovik et al., 2011; Sanghavi et al., 2012; Hollstein and Fischer, 2014; Ding et al., 2016; Wu et al., 2016; Xu et al., 2017). Lidar-based active remote sensing technology provides an attenuated backscatter signal intensity that is processed by designating an extinction-to-backscatter ratio to produce vertical profiles of the aerosol extinction coefficient (Liu et al., 2015; Rosati et al., 2016; Baars et al.,

2021).

245 Two definitions have been proposed and widely used to derive a representative height of wildfire smoke plumes based on the vertical distribution of aerosol extinction coefficient at a given spectral wavelength from active lidar measurements. The concept of “effective *SPH*” can be defined either through smoke aerosol layer boundaries or by considering the complete vertical profile (Fig. 2). One method identifies the topmost height of the plumes according to the geometric boundary of the aerosol layers (*SPH_{top}*). Another approach adopts the average height of the aerosol layers, weighted by the extinction (or backscatter) coefficient that reflects the radiative properties of wildfire smoke particles (*SPH_{ext}*). In this section, we provide a detailed explanation of these two definitions and apply them to the WCL-measured vertical profiles of aerosol extinction coefficient. The height hereinafter is computed in kilometers AGL.

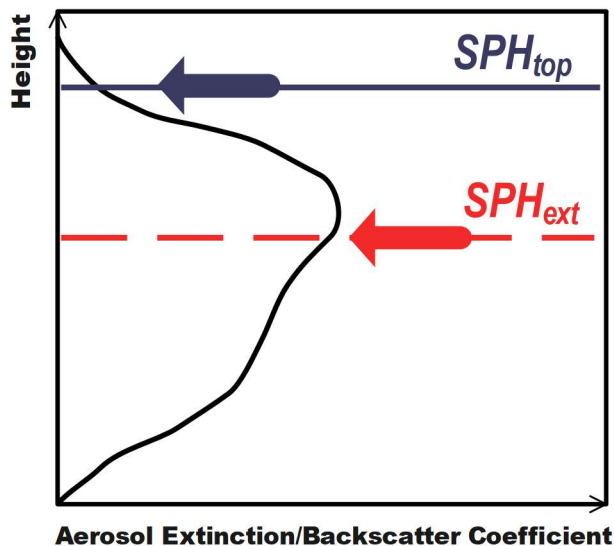


Figure 2: Schematic of two standard *SPH* definitions, *SPH_{top}* and *SPH_{ext}*, proposed in our study.

255 3.1.1 Plume top (*SPH_{top}*)

This definition is built on the wavelet covariance transform (WCT) approach given by Gamage and Hagelberg (1993), which is an automatic algorithmic process to extract geometrical features of interest. Since it can detect the aerosol layer locations of subtle but coherent transitions according to their strength and sign, the WCT analysis has been applied to detect realistic high-resolution atmospheric structures at a variety of vertical spatial scales, such as a well-mixed convective boundary layer top (e.g., Brooks, 2003; Baars et al., 2008) and the edges of lofted aerosol layers (e.g., Davis et al., 2000; Siomos et al., 2017). Here we focus on the derivation for the height of the wildfire smoke plume top, referred to as *SPH_{top}*.

The WCT method is expressed as

$$W_f(a, b) = a^{-1} \int_{z_b}^{z_t} f(z) h\left(\frac{z-b}{a}\right) dz, \quad (1)$$

with a step function, the so-called Haar wavelet $h_{a,b}(z)$, which can be defined as

$$265 \quad h\left(\frac{z-b}{a}\right) = \begin{cases} +1: b - \frac{a}{2} \leq z \leq b \\ -1: b \leq z \leq b + \frac{a}{2} \\ 0: \textit{elsewhere}. \end{cases} \quad (2)$$

In **Eq. (1)**, $f(z)$ is the lidar signal of interest as a function of height AGL, z (is the aerosol extinction profile $\beta(z)$ at 355 nm), and z_t and z_b are the upper and lower limits of the profile. For any arbitrary element of the Haar basis $h_{a,b}(z)$ as shown in **Eq. (2)**, a is the dilation parameter in relation to the spatial spectrum of the function, and b is the translation parameter indicating the location at which the function is centered.

270 The local match or similarity between the Haar wavelet $h_{a,b}(z)$ and the lidar extinction signal $\beta(z)$ is measured in the covariance transform $W_f(a, b)$, which can be interpreted as a pattern search for a sudden jump. Accordingly, the position of the local maxima (i.e., positive peaks) in the return WCT signal approximately marks the layer top; likewise, the position of the local minima (i.e., negative peaks) of the covariance transform $W_f(a, b)$ roughly coincides with the layer bottom. Identification of strong variations in the vertical gradient of the aerosol extinction profile $\beta(z)$ is useful for locating the boundaries between aerosol layers. Following
 275 Michailidis et al. (2021, 2023), we define SPH_{top} as the last positive peak in the corresponding WCT profile from the surface to the upper atmosphere if some physical constraints are satisfied. The optimum value for a affects the number of sufficiently thick aerosol layers that can be retrieved successfully. We therefore limited the minimum acceptable wavelet dilation a to be equal to 54 times the vertical resolution of the aerosol extinction profile $\beta(z)$ at 355 nm, i.e., $a = 162$ m in this study. To filter noise in the return WCT signal, a minimum threshold value is set to 0.05. The values of SPH_{top} are extracted using this approach for both
 280 single-layer and multi-layer aerosol structure smoke plumes, as illustrated in **Figs. S1** and **S2**, respectively.

3.1.2 Extinction-weighted mean plume height (SPH_{ext})

Given an aerosol extinction coefficient profile $\beta(z)$ with n lidar vertical levels, this definition weighs each height AGL interval z_i (in our case $z_i=3$ m) for the i -th level with the height-dependent extinction coefficient $\beta(z_i)$ as described in Koffi et al. (2012), and then calculates the weighted mean height (i.e., SPH_{ext}) as follows:

$$285 \quad SPH_{ext} = \frac{\sum_{i=1}^n \beta(z_i) \cdot z_i}{\sum_{i=1}^n \beta(z_i)}. \quad (3)$$

This method (**Eq. (3)**) has been widely applied in previous literature and is considered ideal for comparisons with the ALH retrieval from passive satellite sensors (Chimot et al., 2018; Kylling et al., 2018; Liu et al., 2019b; Nanda et al., 2020), since it offers a simple and useful means to represent the aerosol vertical distribution as a single height value. For example, in some cases where a single and homogenous (i.e., same particle size and optical properties) aerosol layer is found in the atmosphere, SPH_{ext} indicates
 290 the aerosol layer center of mass. However, when it comes to a vertical structure with multilayer aerosols, SPH_{ext} may be at a vertical level with minimal smoke aerosol loading because smoke plumes are present at multiple heights.

3.2 Lidar–satellite collocation method

When comparing satellite products with observations, a method to collocate the two datasets is required. Even at close range and within short periods, the vertical extent of wildfire smoke plumes can vary substantially. This variation is influenced by factors
 295 such as specific vegetation types and fuel structures, terrain characteristics, or ambient meteorological conditions, during atmospheric transport processes which are more favorable to aerosol aging mechanisms and plume rise behaviors than others

(Paugam et al., 2016; Junghenn Noyes et al., 2022). Passive satellite remote sensing of wildfire *SPH* indirectly measures columnar quantities at a relatively coarse spatial resolution, representing the spatial average of a highly variable pixel area of fire activity and smoke plume behavior. In contrast, active airborne lidar collects instantaneous vertical segments of smoke aerosols only along its flight path, which in turn lacks large-scale spatial representation. Along with the spatial misalignment of collocated pairs, the disparity in sampling time between airplanes and satellites for the same cluster of wildfire plumes, on the order of minutes to days, presents another inherent challenge and thus yields few perfectly matched pairs. Hence, to make comparisons between space- and aircraft-based observing platforms, determining the time interval and distance for collocation pairs of satellite retrievals and lidar measurements requires careful consideration (Junghenn Noyes et al., 2020).

We developed and tested two methods to collocate our aircraft observations with four satellite products (Fig. 3). We expect the collocation method to impact the results because of the spatial heterogeneity of smoke plumes and the range of horizontal resolutions for the four satellite products, from 1 km to 6 km. Another factor is that multiple satellite pixels can coexist in proximity to a single lidar point when satellite orbits and flight legs intersect. When considering these factors, using a single satellite pixel versus an average of pixels in a specific area to collocate satellite products with aircraft observations provides different results for the comparison. Testing the two methods ensures that our comparisons are fair and consistent across the different satellite products. One, the “spatial averaging method”, uses an average of the surrounding satellite pixels around a lidar point, and the other, the “matched pair method”, employs a nearest neighbor search to create a matched lidar–satellite pair.

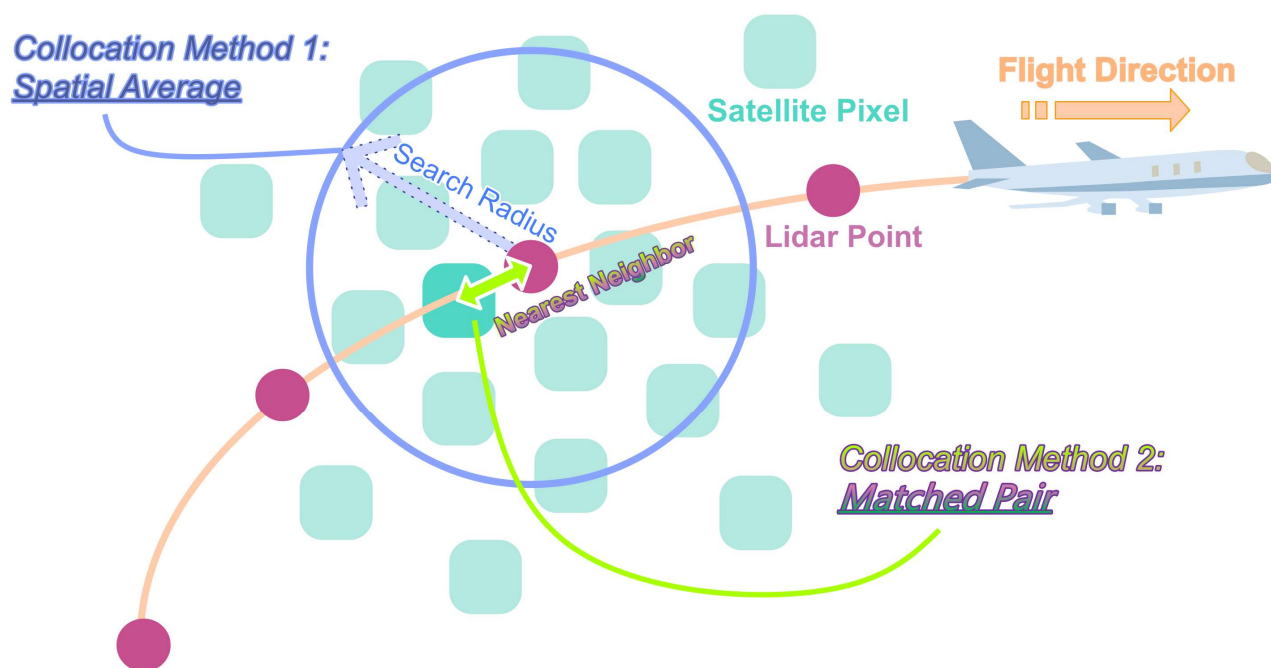


Figure 3: Conceptual diagram of two collocation methods used in our study to pair aircraft observations and passive satellite retrievals. Our collocation criteria are a search radius of 6 km and a sampling time window of 12 minutes.

The spatial averaging method calculates an average value of the satellite retrievals within an area of a fixed search radius around the lidar measurement. For MODIS/MAIAC and MISR/MERLIN, since they have finer spatial resolution (Table 1), this predisposes them to have multiple collocations inside a circular area of a given search radius centered on the lidar point. The values are smoothed because an average value of all satellite retrievals in this circular area for a given sampling time is used for comparison, which is a common practice in the remote sensing field (e.g., Virtanen et al., 2018). Considering that there are fewer collocated

satellite retrievals for the coarse resolution products, such as VIIRS/ASHE and TROPOMI/ALH, within the search area we apply our second collocation method, i.e., the matched pair method. This method is more sensitive to the location of a single satellite pixel coinciding with each point-like airborne lidar measurement. The closest satellite pixel to the nearby lidar point within the given sampling distance and time window is chosen for each match. While using two methods provides the most reliable approach to compare across multiple satellite products, there are still uncertainties associated with satellite-observation comparisons. The main uncertainty sources of collocation mismatch are (1) misalignment between the satellite pixel size and the lidar observation point; (2) wind-driven advection (e.g., a high fire-induced horizontal wind can reach the maximum value of 10 m s^{-1} (Liu et al., 2019c), which can displace fire-related smoke aerosols 3.6 km in 6 minutes); (3) intrinsic positioning and navigation errors. For both methods, we assume that horizontal changes in wildfire smoke plume spread are negligible during short time intervals. It is important to note that each satellite product maintains its native resolution rather than being resampled to a uniform grid for all products. A different collocation method for each satellite product might be used to showcase its spatial characteristics (e.g., to highlight the improvement of finer spatial resolution products).

Both collocation methods require spatiotemporal averaging windows to be selected. A single granule of the VIIRS/ASHE product has the largest pixel size ($6 \text{ km} \times 6 \text{ km}$) with the longest orbit segment scanning period (~ 6 minutes) of all the satellite-derived *SPH* products in **Table 1**. To ensure that adequate collocation pairs are available within one half hour due to rapid wildfire smoke plume activity, we utilized a sampling time window of 12 minutes that corresponds to twice the maximum time span of an orbital swath (one scene). To investigate the effects of search radius size for the two collocation methods, we used 20 sampling distances ranging from 1 km to 20 km. Assuming a worst-case windy environment of 30 m s^{-1} , wildfire smoke aerosol layers could migrate ~ 20 km during the maximum allowed time-interval of 12 minutes. Local *SPH* spatial variability over scales up to ~ 20 km can introduce uncertainty in *SPH* comparisons. In **Fig. S3**, the standard deviation (*STD*) of the multi-sensor satellite *SPH* retrievals around a lidar point (denoted by σ_{SPH}) is calculated to assess the representativeness of the search radius. With increasing distances, all *STD* curves for the satellite-retrieved *SPH* display asymptotic behavior. These values can be interpreted as an upper limit of the *SPH* errors owing to our method of collocation. It is important to optimize the inclusion criteria for the lidar-satellite comparison. For example, a low number of nearby satellite pixel counts shows higher spatial sampling uncertainty, and a low number of one-to-one collocation pairs indicates weaker statistics in calculating the *STD*. Using the mean *STD* ($\overline{\sigma_{SPH}}$) from all collocations, the average number of nearby satellite pixels within a search radius per collocation, and the total number of one-to-one collocation pairs, the best search radius is thus set to 6 km. The collocated satellite *SPH* value is assumed to be representative across the 6 km radius circle centered around the WCL data point, with an average *STD*-calculated uncertainty ($\overline{\sigma_{SPH}}$) of ~ 220 m for MODIS-Terra/MAIAC, ~ 173 m for MAIAC-Aqua/MAIAC, ~ 258 m for MISR/MERLIN, ~ 300 m for VIIRS/ASHE, and ~ 152 m for TROPOMI/ALH.

3.3 Reconstructed lidar vertical cross-sections

When the UWKA flew close-to-perpendicular to the mean wind direction, the consecutive UWKA transects sampled the smoke plumes at different heights over the same latitude or longitude range of the flight trajectory. The UWKA operates at a cruise speed of approximately 90 m s^{-1} , enabling it to capture data from different altitudes and angles. The WCL system uses laser beams to measure the optical properties of the plume, and is limited in its ability to penetrate and sample optically thick smoke. Therefore, the WCL at each flight leg can only provide a partial vertical segment of the smoke plume cross-section, particularly from the lowest flight altitude (i.e., upward scanning lidar).

We reconstructed the vertical structure of wildfire smoke plumes using consecutive WCL transects from different flight legs. This

post-processing approach, using pseudo-vertical profiles of the aerosol extinction coefficient, provides useful lidar-determined
360 *SPH* reference data for comparison with satellite *SPH* products. The reconstruction process involves several key steps following
Deng et al. (2022b):

I. Applying extinction coefficient threshold: Cloud-screened WCL transects are collected from eleven flight tracks
with valid collocation pairs. To separate densely localized fresh smoke from the aged background smoke, an extinction
coefficient threshold of 0.1 km^{-1} is applied. This step helps remove background noise and signal attenuation in the WCL
365 data and ensures a clear distinction between different smoke components.

II. Manual identification of flight legs sampling the same fire smoke plumes: We examine flight track maps and
locate areas where multiple flight legs intersected with a smoke plume from the same fire source.

III. Interpolating discontinuous flight segments to a complete vertical cross-section: To display the vertical cross-
section of the smoke plume more smoothly and aid further analysis and interpretation, scattered lidar points with 2D
370 vertical structure information from multiple flight legs are interpolated to form a continuous line. The interpolation
process relies on the fact that the change in latitude or longitude of the flight tracks is monotonic.

4 Results and discussion

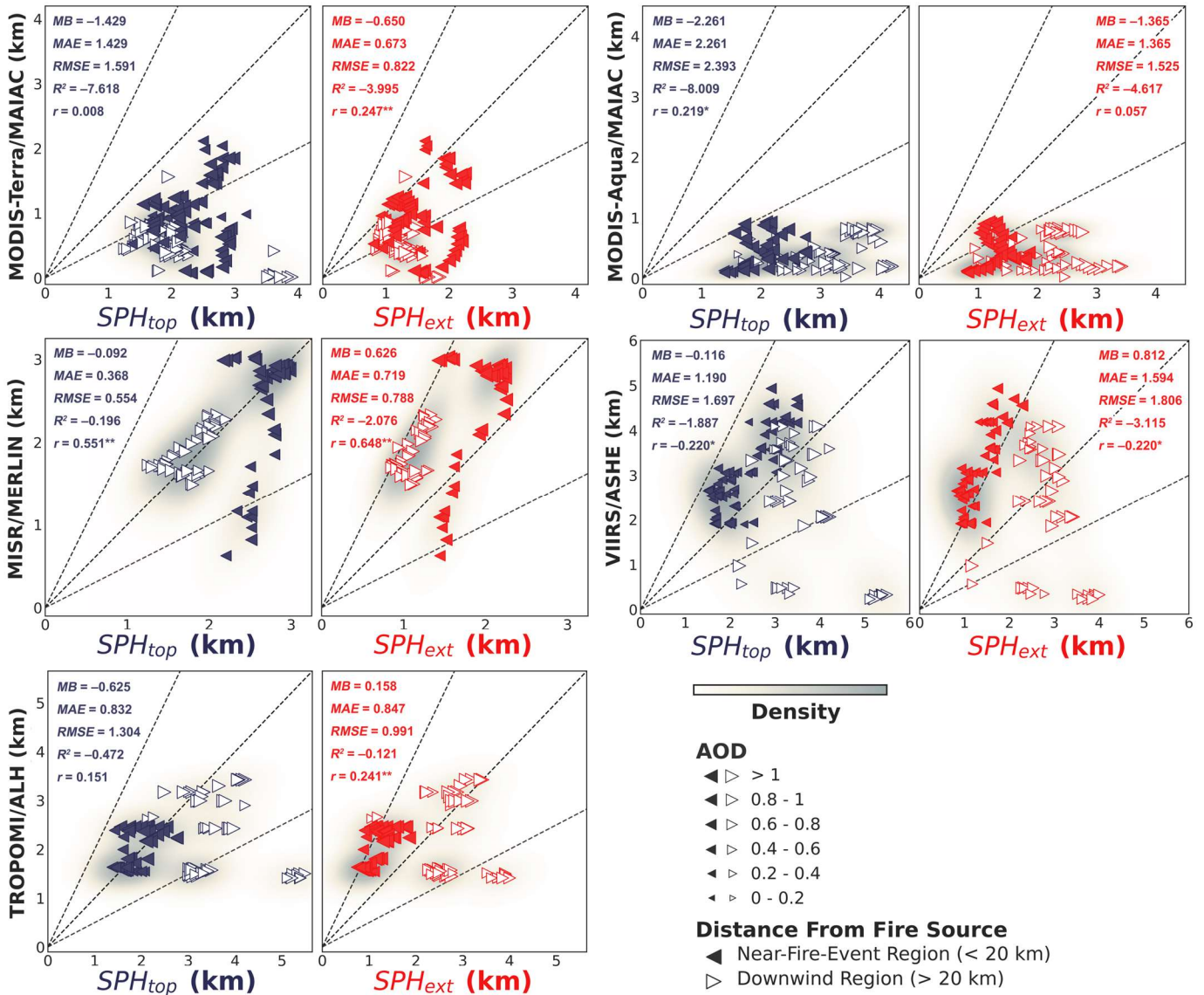
4.1 Evaluation of satellite-retrieved *SPH* using airborne lidar *SPH*

The comparison of satellite-based *SPH* with two distinctive *SPH* definitions using WCL data poses the following question: What
375 other factors influence the *SPH* comparison? To address this question, we considered two factors, distance from the fire and aerosol
loading. Specifically, we defined four categories, “near-fire-event region (distance from the fire source $< 20 \text{ km}$)” or “downwind
region (distance from the fire source $> 20 \text{ km}$)”, and “ $\text{AOD} < 1$ ” or “ $\text{AOD} \geq 1$ ”. We then investigated the relationship between
these factors and the *SPH* comparison for each satellite dataset (**Fig. 4**).

For MODIS-Terra/MAIAC, SPH_{ext} is a better comparison than SPH_{top} for a majority of retrievals not only for the near-fire-event
380 region but also for the downwind region, and the use of SPH_{ext} is not sensitive to significant variability in aerosol loading.
Furthermore, the MAIAC PIH algorithm underestimates *SPH* with increasing AOD in the downwind region. Instead, for MODIS-
Aqua/MAIAC, the retrievals have a high degree of bias compared to lidar-derived *SPH*, with only a few points falling within the
region between the 1:1 and 1:2 lines. The MODIS-Aqua/MAIAC retrievals exhibit more consistency with the definition of SPH_{ext}
near the fire source under high-AOD conditions (when $\text{AOD} \geq 1$). The MISR/MERLIN product has a good agreement between
385 the retrievals and SPH_{top} for the areas in the fire vicinity and downwind, with outliers arising for thin plumes (for lower $\text{AOD} < 0.8$),
potentially due to the unclear boundaries of the smoke plume. This is because the MISR-based automated stereoscopic image
requires distinct plume-like features to provide the complete vertical profile of the smoke plume. The VIIRS/ASHE product
compares better with SPH_{top} than SPH_{ext} . Another interesting finding is that irrespective of AOD values, the ASHE algorithm tends
to overestimate *SPH* for the near-fire-event region, while underestimating *SPH* for the downwind region. Similarly, the
390 TROPOMI/ALH product has lower *SPH* values for the downwind region but higher *SPH* values when close to the fire, regardless
of AOD conditions. The SPH_{top} proves useful to evaluate the TROPOMI/ALH data within the near-fire-event region, whereas the
use of SPH_{ext} is more appropriate for the downwind region if the outliers were removed.

This qualitative analysis sheds light on the factors influencing the comparison between satellite-retrieved *SPH* and lidar-determined
SPH definitions. These findings can aid in the interpretation of *SPH* products from multiple satellite datasets. Additionally, the

395 physical interpretation of the potential biases in the satellite *SPH* algorithms can help design future field campaigns that provide data sets for evaluation and algorithm development. While the qualitative analysis is useful to understand the physical processes impacting the results, we also provided a quantitative evaluation of the satellite *SPH* products using the metrics described in **Appendix A** (results shown on the plots in **Fig. 4**).



400 **Figure 4:** Scatterplots of satellite *SPH* retrievals from MODIS-Terra/MAIAC, MODIS-Aqua/MAIAC, MISR/MERLIN, VIIRS/ASHE, and TROPOMI/ALH versus WCL-determined *SPH* using two different definitions: *SPH_{top}* (left, blue) and *SPH_{ext}* (right, red). Results are for the total collocated lidar–satellite pairs using reconstructed WCL vertical cross-sections during August 2018. Dotted lines denote the ratios of 2:1, 1:1, and 1:2 for reference. The shaded areas show the estimated density of the collocated pairs. Points closer to the fire (within 20 km) are shown as left-pointing triangles, while those farther away, in the downwind area, are shown as right-pointing triangles. The triangle size denotes the corresponding AOD value. Note that the subpanel axes scales for each satellite product are different. Evaluation metrics used to assess the performance of satellite products are *MB* (km) – mean bias; *MAE* (km) – mean absolute error; *RMSE* (km) – root mean square error; *R²* (unitless) – coefficient of determination; and *r* (unitless) – Pearson correlation coefficient (* signifies a *p* value < 0.05, ** indicates a *p* value < 0.01).

The evaluation metrics are calculated using Eqs. (A1) to (A5), where *MB* (km) = 0, *MAE* (km) = 0, *RMSE* (km) = 0, and *r* (unitless) = 1 indicate perfect agreement. The *SPH* values used for metrics are the averages of all successful collocations found in reconstructed lidar vertical cross-sections. Additional statistics for the lidar–satellite comparisons are summarized in **Appendix B**. It should be noted that the collocation method used for comparison is not the same across all of satellite products, where MODIS-

Terra/MAIAC, MODIS-Aqua/MAIAC, and MISR/MERLIN uses the spatial averaging method, and VIIRS/ASHE and TROPOMI/ALH use the matched pair method. Results for both collocation methods for all satellite products are provided in **Tables S1** and **S2**. The statistical comparisons of four *SPH* products derived from passive satellite remote sensing against WCL-determined *SPH* allows us to examine the strengths and limitations of these distinct observational methods. Next, we present an in-depth assessment of the performance of each product based on the quantitative evaluation.

The MAIAC PIH algorithm has low confidence (i.e., large negative R^2 from -8.009 to -3.995 and high $RMSE$ from 0.822 to 2.393) in *SPH* retrievals compared to the WCL *SPH* measurements using two definitions, especially in the afternoon. One reason might be that the MAIAC algorithm cannot achieve strong negative thermal contrast, that is, the smoke pixel (white) is not enough “colder” than the background (dark) in the afternoon when the fire activity is most active. Moreover, assuming an average lapse rate over mountainous terrains instead of more accurate atmospheric temperature profiles from reanalysis data can introduce more uncertainties in *SPH* estimates. A more significant difference between the MODIS/MAIAC *SPH* product and the definition of SPH_{top} is found compared to the definition of SPH_{ext} , indicating the limitation of high enough total AOD to ensure sufficient gaseous absorption constrains its ability to detect SPH_{top} . Therefore, using the definition of SPH_{ext} to evaluate the MODIS/MAIAC product is recommended.

The MISR/MERLIN plume height fluctuates from 0.625 km to 3.029 km, and the corresponding SPH_{top} determined from lidar profiles varies from 1.254 km to 2.982 km. The mean, STD , and quartiles of the collocated MISR/MERLIN *SPH* have relatively small biases compared to SPH_{top} . The MISR/MERLIN product outperforms the other three datasets for capturing SPH_{top} as seen from the lowest values of MB , MAE , and $RMSE$. It also has a moderate positive relationship ($r = 0.551$) with the changes in SPH_{top} . This is anticipated as contrasting features are visible inside plumes and between smoke aerosols and the terrain surface through multiple, angular views, allowing the MISR stereo technique to capture the evolution of wildfire smoke plumes.

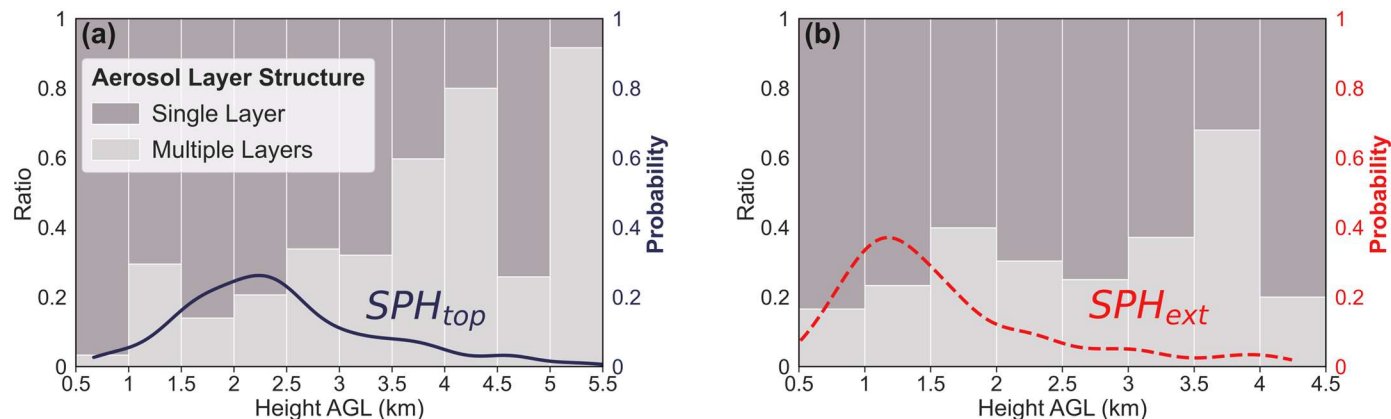
Lee et al. (2015) highlighted that the VIIRS/ASHE product performs well over mountainous areas due to the surface elevation consideration during the retrieval process. Although the mean values and general distribution of both satellite retrievals and lidar observations are fairly close, the VIIRS/ASHE data has a wider spread of values (larger STD), a slight tendency to underestimate SPH_{top} by nearly 116 m, and lower plume height extremes (maximum and minimum plume heights). A fraction within 1.5 km of 14% for VIIRS/ASHE *SPH* leads to some outliers, which are reflected in higher MAE and $RMSE$. These large outlier errors could be attributed to difficulties for passive sensors in measuring the presence of multi-layered aerosols (see **Figs. 7b** and **S4d**), and a potentially high AOD bias over bright surfaces. However, the negative correlation ($r = -0.22$) between the VIIRS/ASHE data and the WCL-determined *SPH* suggests significant discrepancies in their spatial resolution when collocating.

Using the definition of SPH_{ext} , the TROPOMI/ALH product slightly overestimates *SPH* by approximately 158 m, but maintains overall reasonable performance as indicated by the MAE and $RMSE$ values, and a weak positive correlation ($r = 0.241$) with lidar observations. However, this evaluation could be influenced by a limited number of collocations. Choosing the appropriate *SPH* definition to interpret the TROPOMI ALH algorithm depends on a case-by-case basis as shown in the reconstructed lidar curtains (**Sect. 4.3**). When multi-layered structures are detected in the sample cases (**Fig. 7b**), the *SPH* from the TROPOMI ALH algorithm is regarded as the average computation of aerosol optical properties, resulting in a poor comparison with the lidar *SPH*. On the other hand, the TROPOMI ALH algorithm shows encouraging potential for characterizing SPH_{top} in homogenous well-developed smoke layers (**Figs. S4f** and **S4i**). Multilayered aerosols, inaccurate aerosol type detection, and biased UVAI retrievals over bright areas with complex terrain are all potential causes of retrieval uncertainties in the TROPOMI/ALH product.

450 Overall, the discrepancies between passive satellite retrievals and lidar measurements in observing *SPH* primarily stem from their different approaches to characterize smoke aerosol. Passive satellites typically operate under the assumption of a singular aerosol layer within the atmospheric column, a simplification that often fails to account for the presence of multiple layers actively captured by lidars. This divergence creates a challenge in aligning satellite-derived *SPH* data with lidar observations due to the uncertainty in correlating equivalent layers. Further investigation of the smoke plume physics and vertical aerosol distributions are provided
 455 in the following sections using the WCL vertical profiles, including comparisons with passive satellite *SPH* products.

4.2 Leveraging airborne lidar measurements to characterize plume behavior and *SPH*

Through the use of airborne lidar measurements, our study seeks to understand how well a passive satellite remote sensing technique can retrieve *SPH*. The lidar profiles allow for multiple aerosol layers to be sampled, unlike the conventional passive satellite aerosol height retrieval algorithm which presumes the presence of a single, homogeneously distributed aerosol layer
 460 throughout the entire atmosphere. Despite different measurement concepts when it comes to multiple layers of plumes, to ensure comparability between passive retrievals and active observations of smoke plume behavior for ease of calculation, we emphasize the significance of an effective height parameter. The two different *SPH* definitions (**Sect. 3.1**) used to determine this parameter give an indication of the height of the wildfire smoke aerosol distribution as a single number.



465 **Figure 5: Ratios of single-layered and multi-layered aerosol structures in the 0.5 km wide bins using two different WCL-determined *SPH* definitions: (a) *SPH_{top}* and (b) *SPH_{ext}*. Lines indicate probability mass function (PMF). Note that the WCL plume height data are equally binned by setting the bin-width parameter to 0.5 km, and the bins are spread out in the range from 0.5 km to 5.5 km for *SPH_{top}* and in the range from 0.5 km to 4.5 km for *SPH_{ext}*.**

In **Fig. 5**, the height distributions of wildfire smoke plumes during BB-FLUX in August 2018 are shown using two definitions of
 470 lidar-derived *SPH*. Caution should be taken when identifying key criteria used to define *SPH* prior to evaluating the satellite retrievals. This is because *SPH_{top}* (**Fig. 5a**) has a vertical extent spanning from 0.5 km to 5.5 km, with the most common height being approximately 2.25 km. While *SPH_{ext}* (**Fig. 5b**) exhibits a vertical range from 0.5 km to 4.5 km, with its peak observed at roughly 1.2 km. For *SPH* values less than 3.5 km, the occurrence of smoke plumes identified within one single layer is significantly higher than that of multi-layered smoke plumes (> 60% for each height bin), suggesting that the columnar *SPH* values obtained
 475 from satellite retrievals can be compared with those measured via upward-facing lidar profiles, as smoke plumes produced by wildfire typically exhibit a single aerosol layer structure. This finding holds particularly true for wildfires of decreased fire intensity under suppression operations (i.e., some flight dates approach the corresponding fire containment date listed in **Table 2**).

It should be noted that the upward-sampled WCL can only provide a partial vertical segment and not a fully resolved cross-section of the smoke plumes from the lowest flight height due to the restricted lidar laser penetration in optically thick smoke plumes. For

480 instance, when probing the plume centerline, there is complete attenuation of the lidar beam, resulting in a loss of data samples. However, the WCL can successfully delineate the atmosphere on each pass in the less dense portions of smoke plumes. Therefore, the vertical structure of individual smoke plumes reconstructed from airborne WCL measurements yields the vertical profiles of the mean aerosol extinction coefficient, reflecting the average conditions of smoke plumes over multileg UWKA sampling periods (see more details in Sects. 3.3 and 4.3). In terms of lidar-derived SPH biases identified in our study, we observe three main scenarios:
485 (1) underestimation of SPH_{top} (i.e., optically thick plumes limiting vertical extent); (2) overestimation of SPH_{ext} (i.e., the upward-pointing lidar not sampling below aircraft); (3) underestimation of both SPH_{top} and SPH_{ext} in situations where the lidar faces dense smoke above and cannot measure below the aircraft.

4.3 Reconstructed lidar curtain and lidar–satellite comparison

It is necessary to implement post-processing procedures to conduct a comparative analysis between lidar observations and satellite retrievals. Here we present detailed reconstructed lidar vertical cross-sections of aerosol extinction coefficient along with
490 collocated satellite SPH on August 19, 2018, for the morning (0819a, Fig. 6) and afternoon (0819b, Fig. 7) flights. Similar plots are included in Figs. S4 and S5 for each flight. Figs. 6a and 7a demonstrate that the smoke plume coverage of the MISR/MERLIN product aligns well with the manually identified plume area and reveals high-resolution SPH retrievals. In contrast, the MODIS/MAIAC product with the highest spatial resolution displays lower SPH values in general over biomass-burning regions.
495 Meanwhile, both the VIIRS/ASHE product and the TROPOMI/ALH product indicate that higher SPH values are generally shifted towards the downwind region.

The vertical distributions of wildfire smoke aerosols (Figs. 6b and 7b) are useful to visualize the smoke plume structure and provide more information about the physical processes influencing aerosol layering in the atmosphere. A visual comparison of the SPH values from the four satellite products against the WCL is presented in Figs. 6b and 7b. In Fig. 6b, even when faced with
500 intricate aerosol structures, the MISR/MERLIN data is capable of reaching SPH_{top} , except for thin plumes with comparably low AOD values. The MODIS-Terra/MAIAC SPH is similar to SPH_{ext} , although it is unable to distinguish the top of multiple aerosol layers and consequently produces exceptionally low SPH values. Since the reconstructed aerosol vertical cross-section for Fig. 7b is located in the downwind region, there is an increase in SPH_{top} and SPH_{ext} as the distance from the fire increases. We recommend caution when using the MODIS-Aqua/MAIAC product for estimating downwind SPH , as its effectiveness in such scenarios is not
505 always optimal (also refer to Figs. S4b and S4c for more details). This limitation in the MAIAC PIH algorithm has also been reported in previous studies (Lyapustin et al., 2019; Loría-Salazar et al., 2021). Regarding heterogeneous aerosol vertical profiles, the spatial agreement between the collocated VIIRS/ASHE SPH values and the two SPH definitions is poor, despite achieving, on average, a good numerical agreement with SPH_{top} . This is partly due to the coarse spatial resolution of OMPS UVAI data used in the algorithm (~50 km at nadir; ~100 km near the scan edge) not being able to represent finer-scale features. The TROPOMI/ALH
510 data is consistent with the SPH_{ext} values, given the observed overestimation of SPH_{ext} attributable to the elevated flight height. The potential explanation for this phenomenon is that in cases where there may be several layers of smoke aerosols, the retrieved SPH would be the average height of the plume much lower than the height of the optically thick aerosol layer (Michailidis et al., 2023).

According to these results and specific fires studied, the MODIS/MAIAC product struggles with most heterogeneous aerosol structures even in close proximity to active fire sources. Even though the MISR/MERLIN product aims to capture the top boundary
515 of the smoke plume, it can be highly biased in thin plume height estimates with low AOD, or for a more complex aerosol structure with multiple aerosol layers. The challenges observed for the VIIRS/ASHE retrievals are: (1) poor correlation with general trends in lidar measurements; (2) it may not accurately represent complex atmospheric conditions with multiple aerosol layers. Out of the

four satellite *SPH* datasets we investigated, TROPOMI/ALH has the least variance in the retrieved *SPH* across spatial areas. This is not ideal for practical use since real-world wildfire and smoke plume activity varies significantly in space and time. However, elevated smoke layers with a high aerosol loading, over dark surfaces at not very high altitudes are favorable for the TROPOMI ALH algorithm to retrieve vertically localized aerosol layers in the free troposphere (FT). 520

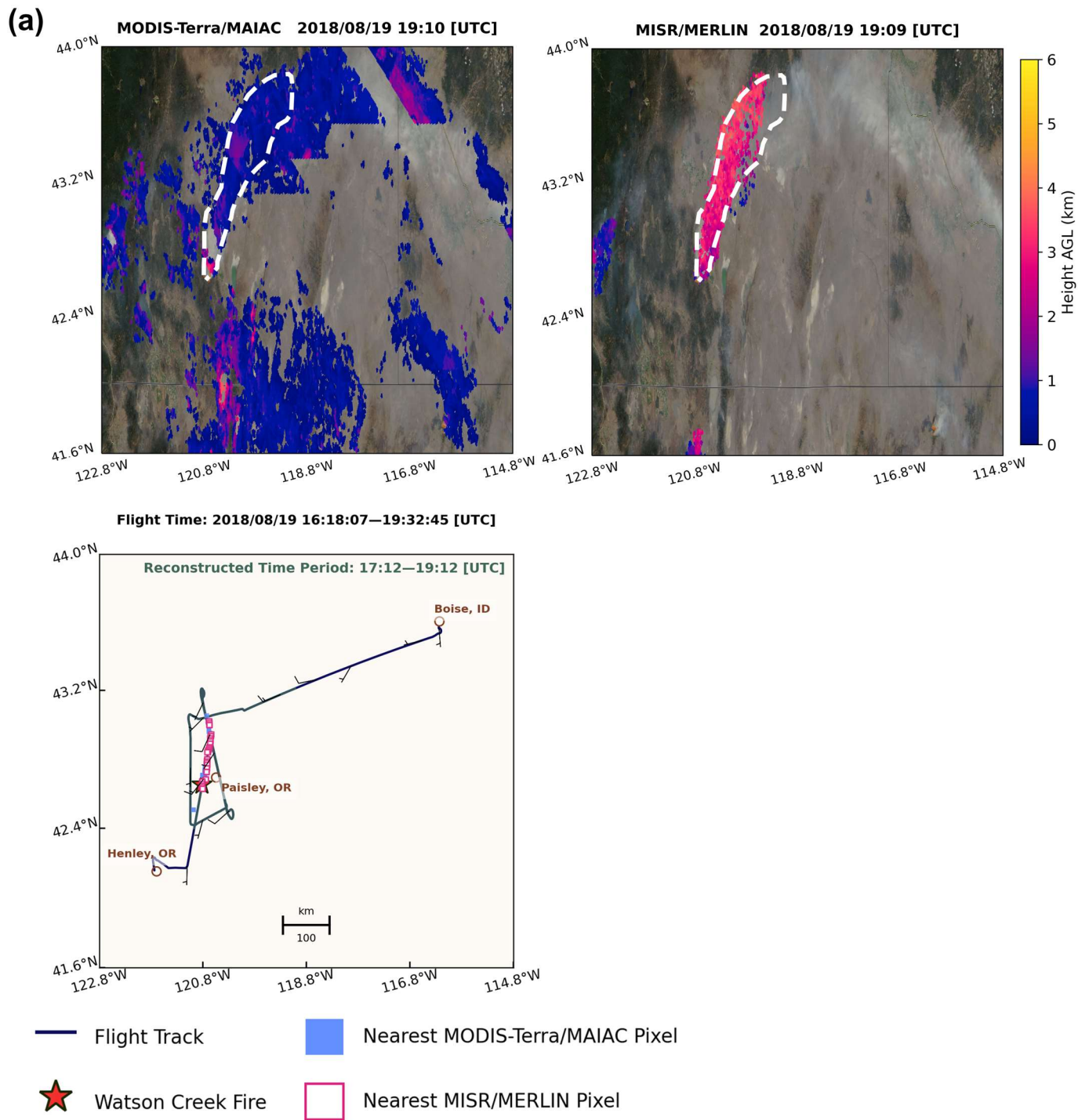
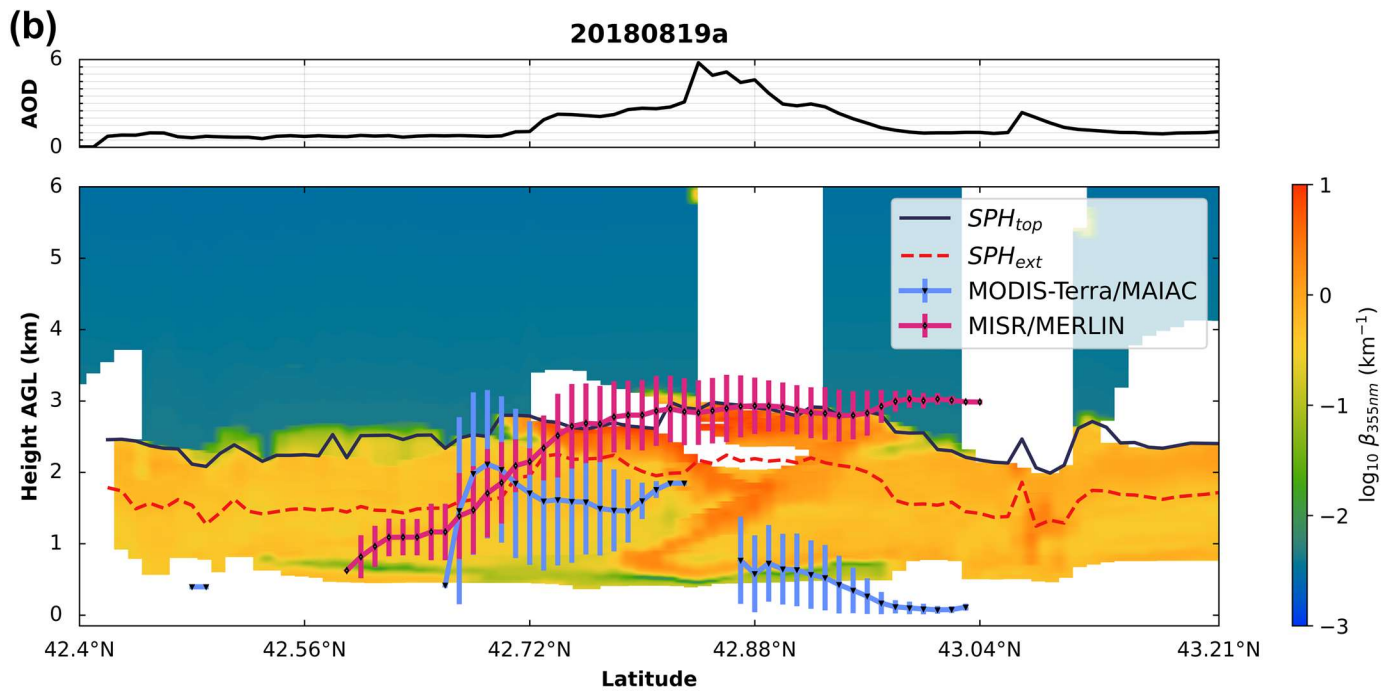


Figure 6: Cont.



525 Figure 6: (a) The nearest satellite pixels of MODIS-Terra/MAIAC and MISR/MERLIN to the corresponding airborne lidar points along
 the 20180819a flight track during the reconstructed time period from 17:12 to 19:12 UTC highlighted in green. Wind barbs are plotted
 along the trajectory with each short barb representing 5 knots and each long barb representing 10 knots. The star symbol indicates the
 center location of the Watson Creek fire taken from the incident report system (Inci-Web). Note that the NASA WorldView MODIS
 Terra true-color (i.e., corrected reflectance) images are shown beneath the satellite-retrieved SPH maps, along with the user-drawn
 530 smoke plume polygons (denoted as the dashed white region). (b) Composite latitude–height cross-sections of the reconstructed WCL
 vertical aerosol extinction coefficient at 355 nm, overlaid with WCL-determined SPH_{top} and SPH_{ext} and the collocated satellite-retrieved
 mean SPH with error bars, for the Watson Creek fire in the morning on August 19, 2018 with the corresponding AOD.

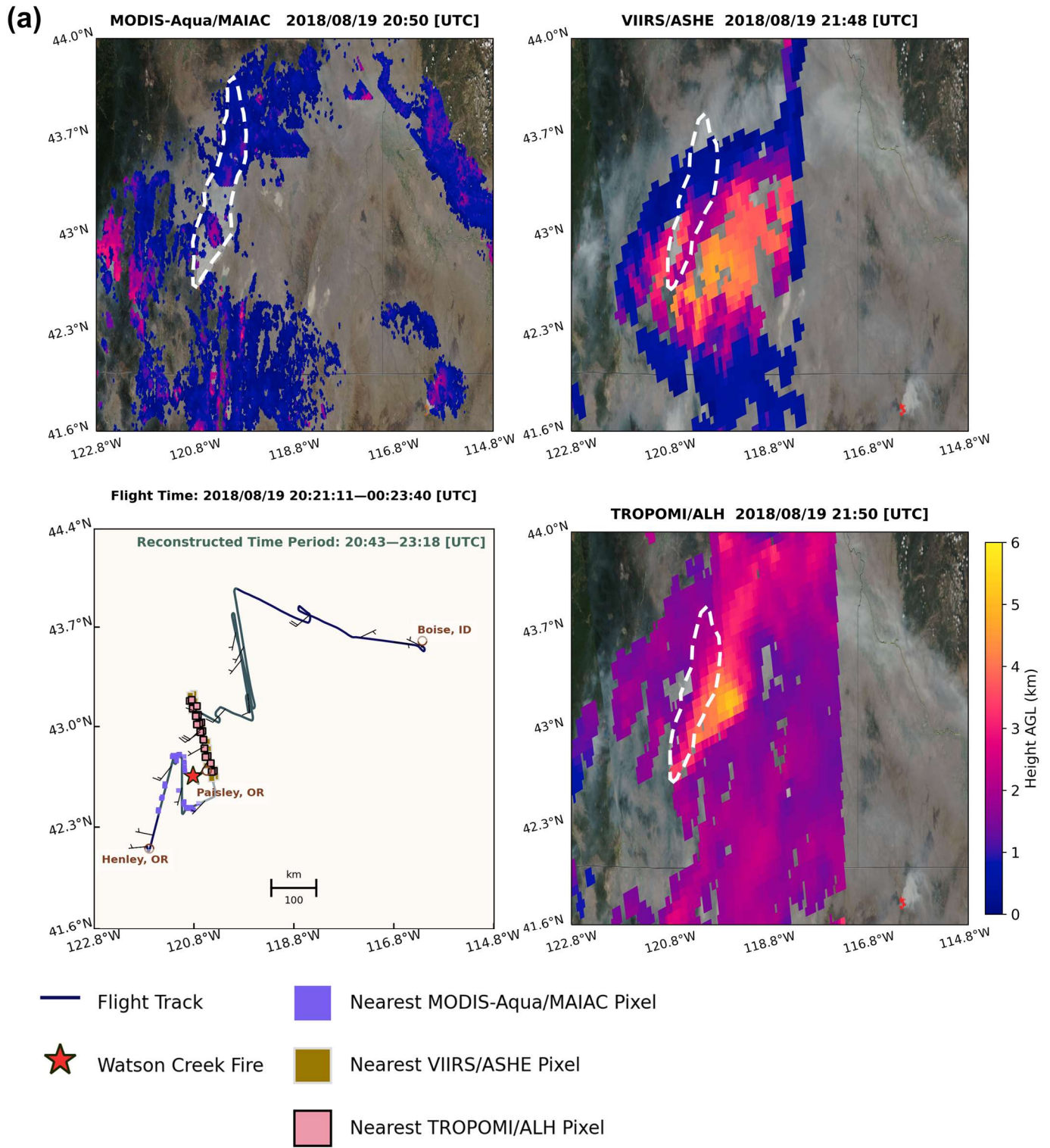
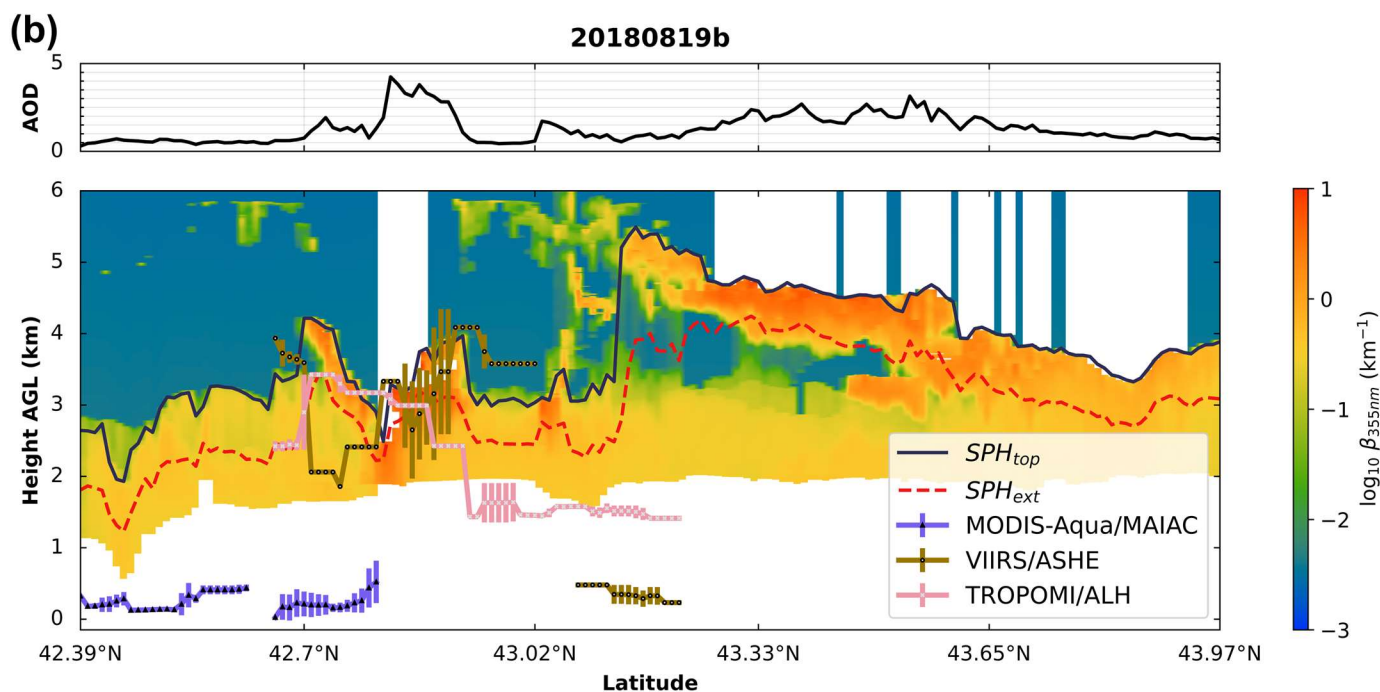


Figure 7: Cont.



535

540

Figure 7: (a) Same as Figure 6a, but for the nearest satellite pixels of MODIS-Aqua/MAIAC, VIIRS/ASHE and TROPOMI/ALH to the corresponding airborne lidar points along the 20180819b flight track during the reconstructed time period from 20:43 to 23:18 UTC highlighted in green. Note that the NASA WorldView true-color images (both MODIS Aqua and VIIRS are used) at the corresponding moment are shown beneath the satellite-retrieved SPH maps, along with the user-drawn smoke plume polygons (denoted as the dashed white region). (b) Same as Figure 6b, but for the Watson Creek fire in the afternoon on August 19, 2018.

4.4 SPH Application

545

550

555

Knowing SPH has additional benefits beyond atmospheric modeling, here we illustrate how SPH can be used to improve our understanding of surface air pollution concentrations and smoke plume dynamics resulting from fire–atmosphere interactions. By using both definitions of SPH , SPH_{top} and SPH_{ext} , additional insights related to plume dynamics can be assessed. How smoke aerosols are vertically distributed throughout the atmosphere plays a dominant role in estimating surface particulate matter (PM) models from satellite AOD products. High-elevation smoke aerosol layers above the planetary boundary layer height ($PBLH$) lead to high column AOD while not elevating the near-surface PM levels. Generally, aerosol concentrations are low in the higher, relatively stable atmospheric layers above the planetary boundary layer (PBL). However, large wildfires can have vigorous buoyant plume cores that lift the smoke plume into the FT or even the stratosphere (Fromm et al., 2019) contributing to elevated aerosol concentrations above the $PBLH$. Based on burned area in **Table 2**, the fires in our study meet the definition of a megafire (10,000–100,000 ha) suggested by Linley et al. (2022), but it should be noted that fire size alone cannot characterize the fire intensity or activity and the resulting smoke plume behavior (Tedim et al., 2018). The ratio of effective SPH to $PBLH$ ($SPH:PBLH$) is an indicator of the AOD and surface PM concentration relationship (Cheeseman et al., 2020). We incorporated the modeled $PBLH$ from the Weather Research and Forecasting Model (WRF) as shown in **Fig. 8**, so we can better understand local meteorology and its impact on wildfire SPH . The WRF model for our use has a domain extending over the WUS with a 4 km spatial resolution, nudged with observations from weather stations as well as balloon soundings. $PBLH$ were recalculated from the WRF simulations using the vertical potential temperature gradient method or the Richardson number method (de Arruda Moreira et al., 2020). The locations and elevations of each balloon sounding station are in **Table S3**, and details of the WRF model configuration are in **Table S4**. Results of the WRF model evaluation are in **Fig. S6**.

560

In **Fig. 8**, there is no clear single pattern for the vertical spread of the smoke plume due to the fire–atmosphere coupling and

boundary-layer turbulence (Sun et al., 2009; Deng et al., 2022b). The difference between SPH_{top} and SPH_{ext} is often greater within a single plume than the differences across different plumes. Based on the wildfire information in **Table 2**, we can qualitatively discuss the differences between $SPH_{top}:PBLH$ and $SPH_{ext}:PBLH$ for each wildfire in terms of their start dates, approximate containment dates, and approximate acres burned. $SPH:PBLH$ characterizes a joint interaction between buoyant plume cores and boundary layer mixing (e.g., entrainment and wind shear). It also depends on other important factors such as the fire size, distance from the fire source, and the fire spread. In some cases, high $SPH_{top}:PBLH$ (> 1) but low $SPH_{ext}:PBLH$ (< 1) occur concurrently, as shown in **Fig. 8**. This means that a higher columnar AOD does not necessarily give rise to the majority of the smoke plume concentrations being above the PBL. For instance, the Watson Creek Fire that started on August 15, 2018, had two flight missions, 0819a and 0819b, and their aviation operation dates were close to the fire start date, compared to 0824a and 0825a flights. The challenging terrain with dense fuel on the ground facilitated rapid fire spread, and the fire was not contained. Therefore, we can expect that the intense fire behavior would generate a higher amount of smoke plumes injected into the FT, where both $SPH_{top}:PBLH$ and $SPH_{ext}:PBLH$ are larger than 1. Five days later, as the fire activity reduced and containment of the fire increased to 15%, there was likely more smoldering and thus lower plume heights. SPH_{ext} reaches a similar level to the $PBLH$, although $SPH_{top}:PBLH$ remains relatively high. When comparing the morning and afternoon SPH patterns, the morning SPH relationships are less complex and potentially easier to model. Where turbulence, convection, and fire-atmosphere interactions contribute to more chaotic plume and PBL dynamics in the afternoon, and the growth rate of the fire exceeds the growth rate of the PBL. The Sheep Creek Fire is an exception due to a timely and consistent fire response making rare SPH behavior in the afternoon possible, where smoke plumes were contained within the PBL. Additionally, a significant portion of the lidar vertical cross-section is missing for the 0823a flight during the South Sugarloaf Fire, as depicted in **Fig. S4g**. In spite of the fire size indicating a megafire (Linley et al., 2022), the absence of the extinction coefficient data as well as in situ sampling in the downwind region (**Table 2**) leads to low estimates of SPH_{top} and SPH_{ext} .

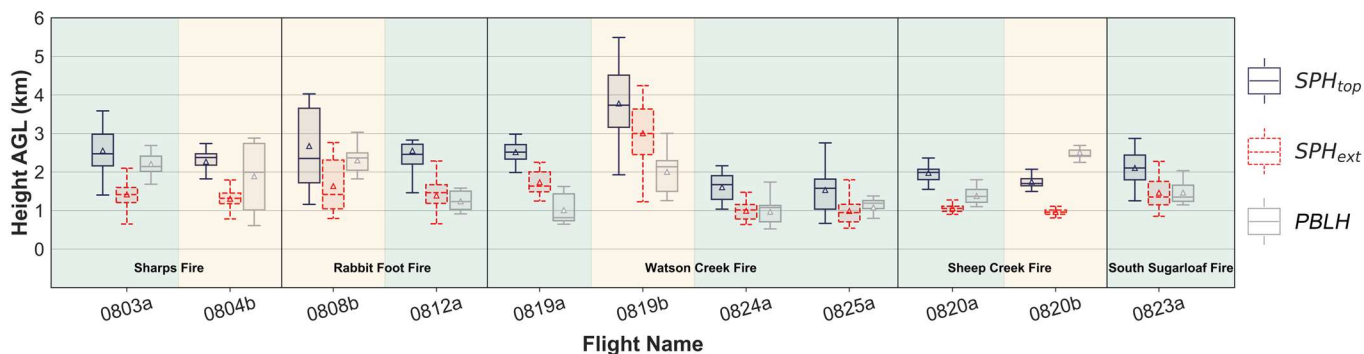


Figure 8: Box plots comparing the 30 min average modeled $PBLH$ (grey) with the WCL-determined SPH using two different definitions (SPH_{top} , blue; SPH_{ext} , red) for the morning (shaded by green) and afternoon (shaded by yellow) flight missions. Each panel represents a single wildfire case. Upper and lower whiskers represent the 95th and 5th percentiles, respectively, while the box spans from the 25th percentile to the 75th percentile. The line inside the box represents the median (the 50th percentile), and the triangle indicates the mean of the range of height values. Note that the range of WCL SPH measurements for both morning (0820a) and afternoon (0820b) flight missions on August 20, 2018, is limited because only a small fraction of flight tracks is considered valid transects for reconstruction.

5 Summary and conclusions

The notion of SPH can be visualized as the vertical displacement from the ground to the upper atmosphere, marking the extent to which smoke plumes ascend. This parameter is vital for simulating the initial stage of plume production and predicting the potential spread of smoke from wildfires (e.g., Walter et al., 2016; Tang et al., 2022). If smoke is emitted above the PBL, it tends to persist longer and travel farther. Smoke emitted within the PBL adversely impacts AQ and increases ground-level air pollution

concentrations.

595 Current efforts to study wildfire *SPH* mainly rely on the use of active lidar data and passive satellite sensor retrievals. However, these instruments face inherent spatial and temporal limitations, such as their inability to swiftly adapt to changes in fire and smoke plume behavior. Nonetheless, fusing multi-satellite products to estimate *SPH* is still an evolving field. Transported smoke aerosols can form complex, multilayer structures, but this study has shown that a single, uniform aerosol layer is encountered more frequently than previously assumed. This means that a single value can be used to describe the height of the aerosol layer. With
600 this more straightforward representation, scientists can more readily incorporate aerosol layer data into climate and AQ models, including our earlier discussion of an “effective *SPH*” concept. We used two *SPH* definitions for comparisons since the *SPH* criterion varies between plume rise retrieval algorithms, given their diverse representations of aerosol vertical allocation that may not sufficiently reflect the real wildfire-associated smoke aerosol layering. We also employed two different collocation methods to provide lidar-satellite collocated pairs. Collocation uncertainties can be caused by the discrepancy between the coarse spatial
605 resolution of the satellite retrieval algorithm and the fine-scale variability of wildfire smoke plume activity detected by high-resolution active lidar measurements.

Results in this paper reaffirmed that uncertainties in multiple satellite-derived *SPH* products arise from different remote sensing techniques (Tosca et al., 2011; Flower and Kahn, 2017). The current state of satellite-based *SPH* products is impacted by significant errors, which we ascribe mostly to either complex, multiple aerosol layers or thin, transparent plumes. The user recommendations
610 and main conclusions drawn from this study are:

- (1) The MAIAC PIH algorithm necessitates careful quality verification since its *SPH* retrievals are routinely lower than the lidar measurements, especially for MODIS/MAIAC-Aqua. We suggest selecting *SPH_{ext}* as a suitable height metric to evaluate the MODIS/MAIAC-Terra product under conditions when the distance from the fire source is < 20 km and for AOD at 355 nm > 1 .
- (2) The MISR plume height climatology is promising to help locate wildfire-associated *SPH_{top}* and provide the best estimates over
615 mountainous terrain. However, as WUS fires have become more frequent since the 2000s, the available MISR/MERLIN datasets are relatively minimal. Some challenges associated with using MISR/MERLIN include the limited timing of MISR overpasses (which only occur in the mid-late morning, local time), and the labor-intensive nature of operating the MINX software to digitize the smoke plumes.
- (3) Both the VIIRS/ASHE and the TROPOMI/ALH products show great potential for characterizing *SPH_{top}* in a single homogenous
620 aerosol-rich layer. An overestimation of *SPH* in the near-fire-event region and an underestimation of *SPH* in the downwind region still prevail. We find that large retrieval errors occur in the studied cases, underscoring the need for a robust quality screening approach related to the UVAI parameterization.

However, the performance evaluation of four satellite *SPH* products presented here indicates only a weak to moderate correlation between passive satellite retrievals and airborne lidar observations. Deploying both passive and active sensors in tandem can offer
625 a synergistic approach, filling gaps in our understanding of fire and smoke plume behavior by utilizing the unique strengths of each method. The lack of synchronization between satellite overpass times and variations in fire activity and aerosol layering is responsible for more than half of the collocation mismatches. It is expected that future satellites, equipped with active or passive sensors, can increase the chances of capturing a large wildfire event at its peak, as exemplified by improved spatial and temporal coverage of the Advanced Baseline Imager (ABI) on geostationary satellites. Notably, NASA’s forthcoming aerosol investigations

630 from space, such as AOS (Atmosphere Observing System), MAIA (Multi-Angle Imager for Aerosols), PACE (Plankton, Aerosol, Cloud, ocean Ecosystem), and TEMPO (Tropospheric Emissions: Monitoring of Pollution), are expected to play a pivotal role in this regard. By integrating data from multiple satellite systems as a potential solution to the synchronization issue, scientists can create a more comprehensive and improved picture of wildfire plume rise.

This study provides a preliminary comparison reference for multiple satellite-based *SPH* applications. Our findings serve to connect smoke transport and AQ forecasting frameworks and future satellite missions that aim to quantify the vertical distribution of aerosols in the atmosphere, similar to the efforts of Raffuse et al. (2012), Solomos et al. (2015), Ke et al. (2021), and Kumar et al. (2022). We therefore encourage conversations between the communities involved in satellite remote sensing and atmospheric modeling to enhance the diversity of perspectives and foster a consensus on the measurement and comprehension of effective *SPH* with greater clarity.

640 **Appendix A. Evaluation metrics for collocated lidar–satellite *SPH* comparison**

We evaluate the performance of a satellite *SPH* product against lidar observations using the following statistics: mean bias (*MB*), mean absolute error (*MAE*), root mean square error (*RMSE*), coefficient of determination (R^2) and Pearson correlation coefficient (r). The metrics are calculated for *SPH* using Eqs. (A1) to (A5):

$$MB = \overline{SPH_{satellite}} - \overline{SPH_{lidar}}, \quad (A1)$$

$$645 \quad MAE = \frac{\sum_{i=1}^N |SPH_{lidar,i} - SPH_{satellite,i}|}{N}, \quad (A2)$$

$$RMSE = \sqrt{\frac{\sum_{i=1}^N (SPH_{lidar,i} - SPH_{satellite,i})^2}{N}}, \quad (A3)$$

$$R^2 = 1 - \frac{\sum_{i=1}^N (SPH_{lidar,i} - SPH_{satellite,i})^2}{\sum_{i=1}^N (SPH_{lidar,i} - \overline{SPH_{lidar}})^2}, \quad (A4)$$

$$r = \frac{\sum_{i=1}^N (SPH_{lidar,i} - \overline{SPH_{lidar}})(SPH_{satellite,i} - \overline{SPH_{satellite}})}{\sqrt{\sum_{i=1}^N (SPH_{lidar,i} - \overline{SPH_{lidar}})^2} \sqrt{\sum_{i=1}^N (SPH_{satellite,i} - \overline{SPH_{satellite}})^2}}, \quad (A5)$$

where $SPH_{lidar,i}$ is the i^{th} collocated lidar measurement, $SPH_{satellite,i}$ is the i^{th} collocated satellite retrieval, $\overline{SPH_{lidar}}$ is the arithmetic mean of the collocated lidar measurements, $\overline{SPH_{satellite}}$ is the arithmetic mean of the collocated satellite retrievals, N is the number of collocated pairs.

MB represents the average bias of a satellite *SPH* product but should be interpreted cautiously because positive and negative errors will cancel out. *MAE* measures the average over the sample absolute differences between lidar measurements and satellite retrievals where all individual differences have equal weight, without considering their direction. *RMSE* is the square root of the average of squared differences between lidar measurements and satellite retrievals. *RMSE* is more useful when large outlier errors are particularly undesirable. Unlike *RMSE*, *MAE* is an unambiguous measure of average error magnitude. R^2 provides a statistical measure of how well a satellite *SPH* retrieval algorithm reflects the real-world conditions as measured by the more direct lidar technique. The closer R^2 is to 1, the more reliable the satellite retrieval is in representing the actual *SPH*. A negative R^2 happens

660 when the performance of the satellite *SPH* product is worse than the mean absolute deviation of the lidar observations. r is a
 665 measure of the strength of a linear association between two variables, indicating that the distribution of both lidar measurements
 and satellite retrievals for *SPH* has a similar trend in the change. The best performance that a satellite *SPH* product would have for
 these evaluation metrics is: MB (km) = 0, MAE (km) = 0, $RMSE$ (km) = 0, R^2 (unitless) = 1, and r (unitless) = 1.

665 **Appendix B. Additional statistical evaluation of four satellite-derived *SPH* products against WCL-determined *SPH* observations. Note that the satellite *SPH* information is only shown in one column to be compared with two distinctive WCL-determined *SPH* definitions. *STD* – standard deviation; *Q25* – lower quartile, 25% of the data lie below this value; *Q50* – median, 50% of the data lie below this value; *Q75* – upper quartile, 25% of the data lie above this value.**

| | WCL-Determined <i>SPH</i> | |
|--|---------------------------|--------------------------|
| | <i>SPH_{top}</i> | <i>SPH_{ext}</i> |
| MODIS-Terra/MAIAC | | |
| # Collocated Pairs (spatial average) | 163 | |
| Lidar Observations Mean \pm 1 <i>STD</i> (km) | 2.162 \pm 0.542 | 1.382 \pm 0.368 |
| Satellite Retrievals Mean \pm 1 <i>STD</i> (km) | 0.733 \pm 0.447 | |
| Lidar Observations ^{Max/Min} (km) | 3.903/1.254 | 2.253/0.800 |
| Satellite Retrievals ^{Max/Min} (km) | 2.114/0.015 | |
| Lidar Observations <i>Q25</i> , <i>Q50</i> , <i>Q75</i> (km) | 1.776, 2.064, 2.508 | 1.131, 1.298, 1.581 |
| Satellite Retrievals <i>Q25</i> , <i>Q50</i> , <i>Q75</i> (km) | 0.438, 0.687, 0.903 | |
| MODIS-Aqua/MAIAC | | |
| # Collocated Pairs (spatial average) | 114 | |
| Lidar Observations Mean \pm 1 <i>STD</i> (km) | 2.686 \pm 0.797 | 1.790 \pm 0.644 |
| Satellite Retrievals Mean \pm 1 <i>STD</i> (km) | 0.425 \pm 0.262 | |
| Lidar Observations ^{Max/Min} (km) | 4.215/1.374 | 3.422/0.800 |
| Satellite Retrievals ^{Max/Min} (km) | 0.935/0.025 | |
| Lidar Observations <i>Q25</i> , <i>Q50</i> , <i>Q75</i> (km) | 2.063, 2.627, 3.350 | 1.274, 1.728, 2.325 |
| Satellite Retrievals <i>Q25</i> , <i>Q50</i> , <i>Q75</i> (km) | 0.192, 0.379, 0.697 | |
| MISR/MERLIN | | |
| # Collocated Pairs (spatial average) | 90 | |
| Lidar Observations Mean \pm 1 <i>STD</i> (km) | 2.216 \pm 0.506 | 1.498 \pm 0.449 |
| Satellite Retrievals Mean \pm 1 <i>STD</i> (km) | 2.124 \pm 0.625 | |
| Lidar Observations ^{Max/Min} (km) | 2.982/1.254 | 2.253/0.853 |
| Satellite Retrievals ^{Max/Min} (km) | 3.029/0.625 | |
| Lidar Observations <i>Q25</i> , <i>Q50</i> , <i>Q75</i> (km) | 1.791, 2.204, 2.648 | 1.129, 1.428, 1.969 |
| Satellite Retrievals <i>Q25</i> , <i>Q50</i> , <i>Q75</i> (km) | 1.658, 2.083, 2.801 | |
| VIIRS/ASHE | | |
| # Collocated Pairs (matched pair) | 130 | |
| Lidar Observations Mean \pm 1 <i>STD</i> (km) | 2.823 \pm 0.999 | 1.895 \pm 0.890 |
| Satellite Retrievals Mean \pm 1 <i>STD</i> (km) | 2.707 \pm 1.165 | |
| Lidar Observations ^{Max/Min} (km) | 5.493/1.497 | 4.003/0.811 |
| Satellite Retrievals ^{Max/Min} (km) | 4.930/0.231 | |

| | | |
|---|---------------------|---------------------|
| Lidar Observations Q_{25}, Q_{50}, Q_{75} (km) | 1.977, 2.904, 3.318 | 1.094, 1.629, 2.489 |
| Satellite Retrievals Q_{25}, Q_{50}, Q_{75} (km) | 2.060, 2.683, 3.579 | |
| TROPOMI/ALH | | |
| # Collocated Pairs (matched pair) | 127 | |
| Lidar Observations Mean ± 1 <i>STD</i> (km) | 2.677 \pm 1.075 | 1.894 \pm 0.936 |
| Satellite Retrievals Mean ± 1 <i>STD</i> (km) | 2.052 \pm 0.588 | |
| Lidar Observations ^{Max} / _{Min} (km) | 5.493/1.374 | 4.003/0.734 |
| Satellite Retrievals ^{Max} / _{Min} (km) | 3.425/1.412 | |
| Lidar Observations Q_{25}, Q_{50}, Q_{75} (km) | 1.718, 2.337, 3.308 | 1.019, 1.542, 2.684 |
| Satellite Retrievals Q_{25}, Q_{50}, Q_{75} (km) | 1.546, 1.802, 2.431 | |

Data availability. The MODIS/MAIAC MCD19A2 Version 6.1 data product can be found at <https://earthdata.nasa.gov>, last access: 10 May 2023. The Atmospheric Sciences Data Center hosts a web-based interface for freely downloading the MISR/MERLIN plume files at <https://10dup05.larc.nasa.gov/merlin/merlin#>, last access: 10 August 2022. The TROPOMI/ALH Level 2 data are publicly available to users via Copernicus Open Access Hub at <https://scihub.copernicus.eu/>, last access: 9 February 2023. The VIIRS/ASHE data can be obtained from the VIIRS Deep Blue Aerosol Group (<https://deepblue.gsfc.nasa.gov/>, last access: 28 July 2022). The BB-FLUX WCL data can be obtained from the official UWKA project website (<http://www.atmos.uwyo.edu/uwka/projects/index.shtml>, last access: 31 October 2022). Balloon sounding data are available from Atmospheric Soundings Wyoming Weather Website (<https://weather.uwyo.edu/upperair/sounding.html>, last access: 22 May 2023).

Author contribution. J.H.: Conceptualization; Investigation; Methodology; Lidar and satellite data curation; Software; Data visualization and analysis; Writing - original draft; Writing - review & editing. S. M. L.: Investigation; Methodology; Writing - review & editing. M.D.: Methodology; Lidar data curation; Writing - review & editing. J. L.: Methodology; Satellite data curation; Writing - review & editing. H. A. H.: Conceptualization; Investigation; Methodology; Supervision; Funding acquisition; Writing - review & editing.

Competing interests. The authors declare that no known conflicts of interest, either financial or interpersonal, could have appeared to influence the work reported in this paper.

Acknowledgements. This material is based on work supported, in part, by the National Science Foundation (NSF) Chemical, Bioengineering, Environmental, and Transport Systems (CBET) under grant number 2048423. We acknowledge high-performance computing support from Cheyenne (doi:10.5065/D6RX99HX) provided by NCAR's Computational and Information Systems Laboratory, sponsored by NSF. We thank the University of Wyoming King Air team for the successful deployment of the 2018 BB-FLUX project (PI: Rainer Volkamer). We acknowledge the use of imagery from the Worldview Snapshots application (<https://wvs.earthdata.nasa.gov>, last access: 15 June 2023), part of the Earth Observing System Data and Information System (EOSDIS). We appreciate the MODIS Adaptive Processing System (MODAPS) Team, the MISR Wildfire Smoke Plume Height Project, and the VIIRS Deep Blue Aerosol Group from NASA, and the TROPOMI Algorithm Team from the ESA for their efforts to create and maintain the satellite data records used in this paper.

References

- Ansmann, A., Baars, H., Chudnovsky, A., Mattis, I., Veselovskii, I., Haarig, M., Seifert, P., Engelmann, R., and Wandinger, U.: Extreme levels of Canadian wildfire smoke in the stratosphere over central Europe on 21–22 August 2017, *Atmospheric Chem. Phys.*, 18, 11831–11845, 2018.
- 695
- Ansmann, A., Ohneiser, K., Mamouri, R.-E., Knopf, D. A., Veselovskii, I., Baars, H., Engelmann, R., Foth, A., Jimenez, C., Seifert, P., and Barja, B.: Tropospheric and stratospheric wildfire smoke profiling with lidar: mass, surface area, CCN, and INP retrieval, *Atmospheric Chem. Phys.*, 21, 9779–9807, <https://doi.org/10.5194/acp-21-9779-2021>, 2021.
- Baars, H., Ansmann, A., Engelmann, R., and Althausen, D.: Continuous monitoring of the boundary-layer top with lidar, *Atmospheric Chem. Phys.*, 8, 7281–7296, <https://doi.org/10.5194/acp-8-7281-2008>, 2008.
- 700
- Baars, H., Radenz, M., Floutsi, A. A., Engelmann, R., Althausen, D., Heese, B., Ansmann, A., Flament, T., Dabas, A., and Traçon, D.: Californian wildfire smoke over Europe: A first example of the aerosol observing capabilities of Aeolus compared to ground-based lidar, *Geophys. Res. Lett.*, 48, e2020GL092194, 2021.
- Boone, J. T., Tosca, M., Galvin, A., Nastan, A., Schurman, D., Nair, P., Davidoff, S., Lombeyda, S., Mushkin, H., and Hendrie, M.: Redesigning for Research: Accessible Data Interaction with MISR Fire Plumes, AGU Fall Meeting Abstracts, GC51E-0840, 2018.
- 705
- Brooks, I. M.: Finding boundary layer top: Application of a wavelet covariance transform to lidar backscatter profiles, *J. Atmospheric Ocean. Technol.*, 20, 1092–1105, 2003.
- Cao, C., De Luccia, F. J., Xiong, X., Wolfe, R., and Weng, F.: Early on-orbit performance of the visible infrared imaging radiometer suite onboard the Suomi National Polar-Orbiting Partnership (S-NPP) satellite, *IEEE Trans. Geosci. Remote Sens.*, 52, 1142–1156, 2013a.
- 710
- Cao, C., Xiong, J., Blonski, S., Liu, Q., Uprety, S., Shao, X., Bai, Y., and Weng, F.: Suomi NPP VIIRS sensor data record verification, validation, and long-term performance monitoring, *J. Geophys. Res. Atmospheres*, 118, 11–664, 2013b.
- Cardil, A., Monedero, S., Ramírez, J., and Silva, C. A.: Assessing and reinitializing wildland fire simulations through satellite active fire data, *J. Environ. Manage.*, 231, 996–1003, 2019.
- 715
- Cheeseman, M., Ford, B., Volckens, J., Lyapustin, A., and Pierce, J.: The relationship between MAIAC smoke plume heights and surface PM, *Geophys. Res. Lett.*, 47, e2020GL088949, 2020.
- Chen, X., Wang, J., Xu, X., Zhou, M., Zhang, H., Garcia, L. C., Colarco, P. R., Janz, S. J., Yorks, J., and McGill, M.: First retrieval of absorbing aerosol height over dark target using TROPOMI oxygen B band: Algorithm development and application for surface particulate matter estimates, *Remote Sens. Environ.*, 265, 112674, 2021.
- 720
- Chimot, J., Veefkind, J. P., Vlemmix, T., De Haan, J. F., Amiridis, V., Proestakis, E., Marinou, E., and Levelt, P. F.: An exploratory study on the aerosol height retrieval from OMI measurements of the 477 nm O₂-O₂ spectral band using a neural network approach, *Atmospheric Meas. Tech.*, 10, 783–809, 2017.
- Chimot, J., Veefkind, J. P., Vlemmix, T., and Levelt, P. F.: Spatial distribution analysis of the OMI aerosol layer height: a pixel-by-pixel comparison to CALIOP observations, *Atmospheric Meas. Tech.*, 11, 2257–2277, 2018.
- 725
- Corradini, S. and Cervino, M.: Aerosol extinction coefficient profile retrieval in the oxygen A-band considering multiple scattering atmosphere. Test case: SCIAMACHY nadir simulated measurements, *J. Quant. Spectrosc. Radiat. Transf.*, 97, 354–380, 2006.
- Csiszar, I., Schroeder, W., Giglio, L., Ellicott, E., Vadrevu, K. P., Justice, C. O., and Wind, B.: Active fires from the Suomi NPP Visible Infrared Imaging Radiometer Suite: Product status and first evaluation results, *J. Geophys. Res. Atmospheres*, 119, 803–816, 2014.
- 730

- Davis, K. J., Gamage, N., Hagelberg, C., Kiemle, C., Lenschow, D., and Sullivan, P.: An objective method for deriving atmospheric structure from airborne lidar observations, *J. Atmospheric Ocean. Technol.*, 17, 1455–1468, 2000.
- de Arruda Moreira, G., Guerrero-Rascado, J. L., Bravo-Aranda, J. A., Foyo-Moreno, I., Cazorla, A., Alados, I., Lyamani, H., Landulfo, E., and Alados-Arboledas, L.: Study of the planetary boundary layer height in an urban environment using a combination of microwave radiometer and ceilometer, *Atmospheric Res.*, 240, 104932, 2020.
- 735 Deng, M., Wang, Z., Volkamer, R., Snider, J. R., Oolman, L., Plummer, D. M., Kille, N., Zarzana, K. J., Lee, C. F., and Campos, T.: Wildfire smoke observations in the western United States from the airborne Wyoming Cloud Lidar during the BB-FLUX project. Part I: Data description and methodology, *J. Atmospheric Ocean. Technol.*, 39, 545–558, 2022a.
- Deng, M., Volkamer, R. M., Wang, Z., Snider, J. R., Kille, N., and Romero-Alvarez, L. J.: Wildfire smoke observations in the western United States from the airborne Wyoming Cloud Lidar during the BB-FLUX project. Part II: Vertical structure and plume injection height, *J. Atmospheric Ocean. Technol.*, 39, 559–572, 2022b.
- 740 Diner, D. J., Beckert, J. C., Reilly, T. H., Bruegge, C. J., Conel, J. E., Kahn, R. A., Martonchik, J. V., Ackerman, T. P., Davies, R., and Gerstl, S. A.: Multi-angle Imaging SpectroRadiometer (MISR) instrument description and experiment overview, *IEEE Trans. Geosci. Remote Sens.*, 36, 1072–1087, 1998.
- 745 Ding, S., Wang, J., and Xu, X.: Polarimetric remote sensing in oxygen A and B bands: sensitivity study and information content analysis for vertical profile of aerosols, *Atmospheric Meas. Tech.*, 9, 2077–2092, 2016.
- Dubovik, O., Herman, M., Holdak, A., Lapyonok, T., Tanré, D., Deuzé, J., Ducos, F., Sinyuk, A., and Lopatin, A.: Statistically optimized inversion algorithm for enhanced retrieval of aerosol properties from spectral multi-angle polarimetric satellite observations, *Atmospheric Meas. Tech.*, 4, 975–1018, 2011.
- 750 Dubuisson, P., Frouin, R., Dessailly, D., Duforêt, L., Léon, J.-F., Voss, K., and Antoine, D.: Estimating the altitude of aerosol plumes over the ocean from reflectance ratio measurements in the O2 A-band, *Remote Sens. Environ.*, 113, 1899–1911, 2009.
- Duforêt, L., Frouin, R., and Dubuisson, P.: Importance and estimation of aerosol vertical structure in satellite ocean-color remote sensing, *Appl. Opt.*, 46, 1107–1119, 2007.
- Flower, V. J. and Kahn, R. A.: Assessing the altitude and dispersion of volcanic plumes using MISR multi-angle imaging from space: Sixteen years of volcanic activity in the Kamchatka Peninsula, Russia, *J. Volcanol. Geotherm. Res.*, 337, 1–15, 2017.
- 755 Fromm, M., Peterson, D., and Di Girolamo, L.: The primary convective pathway for observed wildfire emissions in the upper troposphere and lower stratosphere: A targeted reinterpretation, *J. Geophys. Res. Atmospheres*, 124, 13254–13272, 2019.
- Gamage, N. and Hagelberg, C.: Detection and analysis of microfronts and associated coherent events using localized transforms, *J. Atmospheric Sci.*, 50, 750–756, 1993.
- 760 Geddes, A. and Boesch, H.: Tropospheric aerosol profile information from high-resolution oxygen A-band measurements from space, *Atmospheric Meas. Tech.*, 8, 859–874, 2015.
- Geospatial Multi-Agency Coordination Group, 2019: Historic Perimeters Combined 2000–2018 GeoMAC, available at: <https://data-nifc.opendata.arcgis.com/datasets/nifc::historic-perimeters-combined-2000-2018-geomac/about>, last access: 20 November 2023.
- 765 Goldberg, M. D., Kilcoyne, H., Cikanek, H., and Mehta, A.: Joint Polar Satellite System: The United States next generation civilian polar-orbiting environmental satellite system, *J. Geophys. Res. Atmospheres*, 118, 13–463, 2013.
- Gonzalez-Alonso, L., Val Martin, M., and Kahn, R. A.: Biomass-burning smoke heights over the Amazon observed from space, *Atmospheric Chem. Phys.*, 19, 1685–1702, 2019.
- Gordon, H. R.: Atmospheric correction of ocean color imagery in the Earth Observing System era, *J. Geophys. Res. Atmospheres*, 102, 17081–17106, 1997.
- 770

- Griffin, D., Sioris, C., Chen, J., Dickson, N., Kovachik, A., De Graaf, M., Nanda, S., Veefkind, P., Dammers, E., and McLinden, C. A.: The 2018 fire season in North America as seen by TROPOMI: aerosol layer height intercomparisons and evaluation of model-derived plume heights, *Atmospheric Meas. Tech.*, 13, 1427–1445, 2020.
- Hollstein, A. and Fischer, J.: Retrieving aerosol height from the oxygen A band: a fast forward operator and sensitivity study concerning spectral resolution, instrumental noise, and surface inhomogeneity, *Atmospheric Meas. Tech.*, 7, 1429–1441, 2014.
- 775 Hsu, N. C., Herman, J., Bhartia, P., Seftor, C., Torres, O., Thompson, A., Gleason, J., Eck, T., and Holben, B.: Detection of biomass burning smoke from TOMS measurements, *Geophys. Res. Lett.*, 23, 745–748, 1996.
- Hsu, N. C., Herman, J., Torres, O., Holben, B., Tanre, D., Eck, T., Smirnov, A., Chatenet, B., and Lavenu, F.: Comparisons of the TOMS aerosol index with Sun-photometer aerosol optical thickness: Results and applications, *J. Geophys. Res. Atmospheres*, 104, 6269–6279, 1999.
- 780 Ichoku, C., Kahn, R., and Chin, M.: Satellite contributions to the quantitative characterization of biomass burning for climate modeling, *Atmospheric Res.*, 111, 1–28, 2012.
- Jeong, M. and Hsu, N. C.: Retrievals of aerosol single-scattering albedo and effective aerosol layer height for biomass-burning smoke: Synergy derived from “A-Train” sensors, *Geophys. Res. Lett.*, 35, 2008.
- 785 Jeong, U., Tsay, S.-C., Hsu, N. C., Giles, D. M., Cooper, J. W., Lee, J., Swap, R. J., Holben, B. N., Butler, J. J., and Wang, S.-H.: Simultaneous retrievals of biomass burning aerosols and trace gases from the ultraviolet to near-infrared over northern Thailand during the 2019 pre-monsoon season, *Atmospheric Chem. Phys.*, 22, 11957–11986, 2022.
- Junghenn Noyes, K. T., Kahn, R. A., Sedlacek, A., Kleinman, L., Limbacher, J. A., and Li, Z.: Wildfire smoke particle properties and evolution, from space-based multi-angle imaging, *Remote Sens.*, 12, 769, 2020.
- 790 Junghenn Noyes, K. T., Kahn, R. A., Limbacher, J. A., and Li, Z.: Canadian and Alaskan wildfire smoke particle properties, their evolution, and controlling factors, from satellite observations, *Atmospheric Chem. Phys.*, 22, 10267–10290, 2022.
- Kahn, R. A.: A Global Perspective on Wildfires, *Eos*, 101, <https://doi.org/10.1029/2020EO138260>, 2020.
- Kahn, R. A., Li, W., Moroney, C., Diner, D. J., Martonchik, J. V., and Fishbein, E.: Aerosol source plume physical characteristics from space-based multiangle imaging, *J. Geophys. Res. Atmospheres*, 112, 2007.
- 795 Kahn, R. A., Chen, Y., Nelson, D. L., Leung, F., Li, Q., Diner, D. J., and Logan, J. A.: Wildfire smoke injection heights: Two perspectives from space, *Geophys. Res. Lett.*, 35, 2008.
- Ke, Z., Wang, Y., Zou, Y., Song, Y., and Liu, Y.: Global Wildfire Plume-Rise Data Set and Parameterizations for Climate Model Applications, *J. Geophys. Res. Atmospheres*, 126, e2020JD033085, 2021.
- Koffi, B., Schulz, M., Bréon, F., Griesfeller, J., Winker, D., Balkanski, Y., Bauer, S., Berntsen, T., Chin, M., and Collins, W. D.: Application of the CALIOP layer product to evaluate the vertical distribution of aerosols estimated by global models: AeroCom phase I results, *J. Geophys. Res. Atmospheres*, 117, 2012.
- 800 Kumar, A., Pierce, R. B., Ahmadov, R., Pereira, G., Freitas, S., Grell, G., Schmidt, C., Lenzen, A., Schwarz, J. P., and Perring, A. E.: Simulating wildfire emissions and plume rise using geostationary satellite fire radiative power measurements: a case study of the 2019 Williams Flats fire, *Atmospheric Chem. Phys.*, 22, 10195–10219, 2022.
- 805 Kylling, A., Vandenbussche, S., Capelle, V., Cuesta, J., Klüser, L., Lelli, L., Popp, T., Stebel, K., and Veefkind, P.: Comparison of dust-layer heights from active and passive satellite sensors, *Atmospheric Meas. Tech.*, 11, 2911–2936, 2018.
- Labonne, M., Bréon, F., and Chevallier, F.: Injection height of biomass burning aerosols as seen from a spaceborne lidar, *Geophys. Res. Lett.*, 34, 2007.
- Lee, J., Hsu, N. C., Bettenhausen, C., Sayer, A. M., Seftor, C. J., and Jeong, M. -J.: Retrieving the height of smoke and dust aerosols by synergistic use of VIIRS, OMPS, and CALIOP observations, *J. Geophys. Res. Atmospheres*, 120, 8372–8388, 2015.
- 810

- Lee, J., Hsu, N. C., Bettenhausen, C., Sayer, A. M., Seftor, C. J., Jeong, M.-J., Tsay, S.-C., Welton, E. J., Wang, S.-H., and Chen, W.-N.: Evaluating the height of biomass burning smoke aerosols retrieved from synergistic use of multiple satellite sensors over Southeast Asia, *Aerosol Air Qual. Res.*, 16, 2831, 2016.
- 815 Lee, J., Hsu, N. C., Sayer, A. M., Seftor, C. J., and Kim, W. V.: Aerosol layer height with enhanced spectral coverage achieved by synergy between VIIRS and OMPS-NM measurements, *IEEE Geosci. Remote Sens. Lett.*, 18, 949–953, 2020.
- Linley, G. D., Jolly, C. J., Doherty, T. S., Geary, W. L., Armenteras, D., Belcher, C. M., Bliege Bird, R., Duane, A., Fletcher, M., and Giorgis, M. A.: What do you mean, ‘megafire’?, *Glob. Ecol. Biogeogr.*, 31, 1906–1922, 2022.
- Liu, D., Chen, S., Cheng, C., Barker, H. W., Dong, C., Ke, J., Wang, S., and Zheng, Z.: Analysis of global three-dimensional aerosol structure with spectral radiance matching, *Atmospheric Meas. Tech.*, 12, 6541–6556, 2019a.
- 820 Liu, M., Lin, J., Boersma, K. F., Pinardi, G., Wang, Y., Chimot, J., Wagner, T., Xie, P., Eskes, H., and Van Roozendaal, M.: Improved aerosol correction for OMI tropospheric NO₂ retrieval over East Asia: constraint from CALIOP aerosol vertical profile, *Atmospheric Meas. Tech.*, 12, 1–21, 2019b.
- Liu, Y., Kochanski, A., Baker, K. R., Mell, W., Linn, R., Paugam, R., Mandel, J., Fournier, A., Jenkins, M. A., and Goodrick, S.: Fire behaviour and smoke modelling: model improvement and measurement needs for next-generation smoke research and
825 forecasting systems, *Int. J. Wildland Fire*, 28, 570–588, 2019c.
- Liu, Z., Winker, D., Omar, A., Vaughan, M., Kar, J., Trepte, C., Hu, Y., and Schuster, G.: Evaluation of CALIOP 532 nm aerosol optical depth over opaque water clouds, *Atmospheric Chem. Phys.*, 15, 1265–1288, 2015.
- Loría-Salazar, S. M., Sayer, A. M., Barnes, J., Huang, J., Flynn, C., Lareau, N., Lee, J., Lyapustin, A., Redemann, J., Welton, E. J., Wilkins, J. L., ... & Holmes, H. A.: Evaluation of Novel NASA Moderate Resolution Imaging Spectroradiometer and Visible
830 Infrared Imaging Radiometer Suite Aerosol Products and Assessment of Smoke Height Boundary Layer Ratio During Extreme Smoke Events in the Western USA, *J. Geophys. Res. Atmospheres*, 126, e2020JD034180, <https://doi.org/10.1029/2020JD034180>, 2021.
- Lu, Z., Wang, J., Xu, X., Chen, X., Kondragunta, S., Torres, O., Wilcox, E. M., and Zeng, J.: Hourly mapping of the layer height of thick smoke plumes over the western US in 2020 severe fire season, *Front. Remote Sens.*, 2, 766628, 2021.
- 835 Lyapustin, A., Wang, Y., and Frey, R.: An automatic cloud mask algorithm based on time series of MODIS measurements, *J. Geophys. Res. Atmospheres*, 113, 2008.
- Lyapustin, A., Wang, Y., Korkin, S., Kahn, R., and Winker, D.: MAIAC thermal technique for smoke injection height from MODIS, *IEEE Geosci. Remote Sens. Lett.*, 17, 730–734, 2019.
- Mamouri, R.-E. and Ansmann, A.: Potential of polarization lidar to provide profiles of CCN-and INP-relevant aerosol parameters,
840 *Atmospheric Chem. Phys.*, 16, 5905–5931, 2016.
- Mardi, A. H., Dadashazar, H., MacDonald, A. B., Braun, R. A., Crosbie, E., Xian, P., Thorsen, T. J., Coggon, M. M., Fenn, M. A., and Ferrare, R. A.: Biomass burning plumes in the vicinity of the California coast: Airborne characterization of physicochemical properties, heating rates, and spatiotemporal features, *J. Geophys. Res. Atmospheres*, 123, 13–560, 2018.
- McGill, M. J., Yorks, J. E., Scott, V. S., Kupchock, A. W., and Selmer, P. A.: The cloud-aerosol transport system (CATS): a
845 technology demonstration on the international space station, *Lidar remote sensing for environmental monitoring XV*, 34–39, 2015.
- Michailidis, K., Koukouli, M.-E., Siomos, N., Balis, D., Tuinder, O., Tilstra, L. G., Mona, L., Pappalardo, G., and Bortoli, D.: First validation of GOME-2/MetOp absorbing aerosol height using EARLINET lidar observations, *Atmospheric Chem. Phys.*, 21, 3193–3213, 2021.

- 850 Michailidis, K., Koukouli, M.-E., Balis, D., Veefkind, J. P., De Graaf, M., Mona, L., Papagianopoulos, N., Pappalardo, G., Tsikoudi, I., and Amiridis, V.: Validation of the TROPOMI/S5P aerosol layer height using EARLINET lidars, *Atmospheric Chem. Phys.*, 23, 1919–1940, 2023.
- Moroney, C., Davies, R., and Muller, J.-P.: Operational retrieval of cloud-top heights using MISR data, *IEEE Trans. Geosci. Remote Sens.*, 40, 1532–1540, 2002.
- 855 Muller, J.-P., Mandanayake, A., Moroney, C., Davies, R., Diner, D. J., and Paradise, S.: MISR stereoscopic image matchers: Techniques and results, *IEEE Trans. Geosci. Remote Sens.*, 40, 1547–1559, 2002.
- Nanda, S., Veefkind, J. P., De Graaf, M., Sneep, M., Stammes, P., De Haan, J. F., Sanders, A. F., Apituley, A., Tuinder, O., and Levelt, P. F.: A weighted least squares approach to retrieve aerosol layer height over bright surfaces applied to GOME-2 measurements of the oxygen A band for forest fire cases over Europe, *Atmospheric Meas. Tech.*, 11, 3263–3280, 2018a.
- 860 Nanda, S., De Graaf, M., Sneep, M., De Haan, J. F., Stammes, P., Sanders, A. F., Tuinder, O., Veefkind, J. P., and Levelt, P. F.: Error sources in the retrieval of aerosol information over bright surfaces from satellite measurements in the oxygen A band, *Atmospheric Meas. Tech.*, 11, 161–175, 2018b.
- Nanda, S., De Graaf, M., Veefkind, J. P., Ter Linden, M., Sneep, M., De Haan, J., and Levelt, P. F.: A neural network radiative transfer model approach applied to the Tropospheric Monitoring Instrument aerosol height algorithm, *Atmospheric Meas. Tech.*, 865 12, 6619–6634, 2019.
- Nanda, S., De Graaf, M., Veefkind, J. P., Sneep, M., ter Linden, M., Sun, J., and Levelt, P. F.: A first comparison of TROPOMI aerosol layer height (ALH) to CALIOP data, *Atmospheric Meas. Tech.*, 13, 3043–3059, 2020.
- Nastan, A., Val, S., Tosca, M., Galvin, A., Ainsworth, H., and Diner, D. J.: Enabling New Research with MISR Wildfire Plume Height Project Data: The MISR Enhanced Research and Lookup INterface (MERLIN), *AGU Fall Meeting Abstracts*, A14F-870 01, 2022.
- Nelson, D. L., Chen, Y., Kahn, R. A., Diner, D. J., and Mazzone, D.: Example applications of the MISR INteractive eXplorer (MINX) software tool to wildfire smoke plume analyses, *Remote sensing of fire: Science and application*, 65–75, 2008.
- Nelson, D. L., Garay, M. J., Kahn, R. A., and Dunst, B. A.: Stereoscopic height and wind retrievals for aerosol plumes with the MISR INteractive eXplorer (MINX), *Remote Sens.*, 5, 4593–4628, 2013.
- 875 Paugam, R., Wooster, M., Atherton, J., Freitas, S., Schultz, M., and Kaiser, J.: Development and optimization of a wildfire plume rise model based on remote sensing data inputs—Part 2, *Atmospheric Chem. Phys. Discuss.*, 15, 9815–9895, 2015.
- Paugam, R., Wooster, M., Freitas, S., and Val Martin, M.: A review of approaches to estimate wildfire plume injection height within large-scale atmospheric chemical transport models, *Atmospheric Chem. Phys.*, 16, 907–925, 2016.
- Raffuse, S. M., Craig, K. J., Larkin, N. K., Strand, T. T., Sullivan, D. C., Wheeler, N. J., and Solomon, R.: An evaluation of 880 modeled plume injection height with satellite-derived observed plume height, *Atmosphere*, 3, 103–123, 2012.
- Rosati, B., Herrmann, E., Bucci, S., Fierli, F., Cairo, F., Gysel, M., Tillmann, R., Größ, J., Gobbi, G. P., and Di Liberto, L.: Studying the vertical aerosol extinction coefficient by comparing in situ airborne data and elastic backscatter lidar, *Atmospheric Chem. Phys.*, 16, 4539–4554, 2016.
- Salomonson, V. V., Barnes, W., Xiong, J., Kempler, S., and Masuoka, E.: An overview of the Earth Observing System MODIS 885 instrument and associated data systems performance, *IEEE International Geoscience and Remote Sensing Symposium*, 1174–1176, 2002.
- Sanders, A. F., De Haan, J. F., Sneep, M., Apituley, A., Stammes, P., Vieitez, M., Tilstra, L., Koning, C., and Veefkind, J. P.: Evaluation of the operational Aerosol Layer Height retrieval algorithm for Sentinel-5 Precursor: application to O 2 A band observations from GOME-2A, *Atmospheric Meas. Tech.*, 8, 4947–4977, 2015.

- 890 Sanders, A. F., De Haan, J. F., and Veefkind, J. P.: Retrieval of aerosol height from the oxygen A band with TROPOMI, *Proc. Adv. Atmospheric Sci. Appl. Bruges Belg.*, 18–22, 2012.
- Sanghavi, S., Martonchik, J., Landgraf, J., and Platt, U.: Retrieval of the optical depth and vertical distribution of particulate scatterers in the atmosphere using O 2 A-and B-band SCIAMACHY observations over Kanpur: a case study, *Atmospheric Meas. Tech.*, 5, 1099–1119, 2012.
- 895 Schroeder, W., Oliva, P., Giglio, L., and Csiszar, I. A.: The New VIIRS 375 m active fire detection data product: Algorithm description and initial assessment, *Remote Sens. Environ.*, 143, 85–96, 2014.
- Sicard, M., Granados-Muñoz, M. J., Alados-Arboledas, L., Barragán, R., Bedoya-Velásquez, A. E., Benavent-Oltra, J. A., Bortoli, D., Comerón, A., Córdoba-Jabonero, C., and Costa, M. J.: Ground/space, passive/active remote sensing observations coupled with particle dispersion modelling to understand the inter-continental transport of wildfire smoke plumes, *Remote Sens. Environ.*, 232, 111294, 2019.
- 900 Siomos, N., Balis, D. S., Poupkou, A., Liora, N., Dimopoulos, S., Melas, D., Giannakaki, E., Filioglou, M., Basart, S., and Chaikovskiy, A.: Investigating the quality of modeled aerosol profiles based on combined lidar and sunphotometer data, *Atmospheric Chem. Phys.*, 17, 7003–7023, <https://doi.org/10.5194/acp-17-7003-2017>, 2017.
- Solomon, S., Dube, K., Stone, K., Yu, P., Kinnison, D., Toon, O. B., Strahan, S. E., Rosenlof, K. H., Portmann, R., and Davis, S.: 905 On the stratospheric chemistry of midlatitude wildfire smoke, *Proc. Natl. Acad. Sci.*, 119, e2117325119, 2022.
- Solomos, S., Amiridis, V., Zanis, P., Gerasopoulos, E., Sofiou, F., Herekakis, T., Brioude, J., Stohl, A., Kahn, R., and Kontoes, C.: Smoke dispersion modeling over complex terrain using high resolution meteorological data and satellite observations–The FireHub platform, *Atmos. Environ.*, 119, 348–361, 2015.
- Sun, R., Krueger, S. K., Jenkins, M. A., Zulauf, M. A., and Charney, J. J.: The importance of fire–atmosphere coupling and 910 boundary-layer turbulence to wildfire spread, *Int. J. Wildland Fire*, 18, 50–60, 2009.
- Tang, W., Emmons, L. K., Buchholz, R. R., Wiedinmyer, C., Schwantes, R. H., He, C., Kumar, R., Pfister, G. G., Worden, H. M., and Hornbrook, R. S.: Effects of fire diurnal variation and plume rise on US Air quality during FIREX-AQ and WE-CAN Based on the multi-scale infrastructure for chemistry and aerosols (MUSICAv0), *J. Geophys. Res. Atmospheres*, 127, e2022JD036650, 2022.
- 915 Tedim, F., Leone, V., Amraoui, M., Bouillon, C., Coughlan, M. R., Delogu, G. M., Fernandes, P. M., Ferreira, C., McCaffrey, S., McGee, T. K., Parente, J., Paton, D., Pereira, M. G., Ribeiro, L. M., Viegas, D. X., and Xanthopoulos, G.: Defining Extreme Wildfire Events: Difficulties, Challenges, and Impacts, *Fire*, 1, <https://doi.org/10.3390/fire1010009>, 2018.
- Torres, O., Bhartia, P., Herman, J., Ahmad, Z., and Gleason, J.: Derivation of aerosol properties from satellite measurements of backscattered ultraviolet radiation: Theoretical basis, *J. Geophys. Res. Atmospheres*, 103, 17099–17110, 1998.
- 920 Tosca, M., Randerson, J., Zender, C., Nelson, D., Diner, D., and Logan, J.: Dynamics of fire plumes and smoke clouds associated with peat and deforestation fires in Indonesia, *J. Geophys. Res. Atmospheres*, 116, 2011.
- Toth, T. D., Zhang, J., Reid, J. S., and Vaughan, M. A.: A bulk-mass-modeling-based method for retrieving particulate matter pollution using CALIOP observations, *Atmospheric Meas. Tech.*, 12, 1739–1754, 2019.
- Val Martin, M., Kahn, R. A., and Tosca, M. G.: A global analysis of wildfire smoke injection heights derived from space-based 925 multi-angle imaging, *Remote Sens.*, 10, 1609, 2018.
- Veefkind, J. P., Aben, I., McMullan, K., Förster, H., De Vries, J., Otter, G., Claas, J., Eskes, H., De Haan, J., and Kleipool, Q.: TROPOMI on the ESA Sentinel-5 Precursor: A GMES mission for global observations of the atmospheric composition for climate, air quality and ozone layer applications, *Remote Sens. Environ.*, 120, 70–83, 2012.

- 930 Virtanen, T. H., Kolmonen, P., Sogacheva, L., Rodríguez, E., Saponaro, G., and de Leeuw, G.: Collocation mismatch uncertainties in satellite aerosol retrieval validation, *Atmospheric Meas. Tech.*, 11, 925–938, 2018.
- Walter, C., Freitas, S. R., Kottmeier, C., Kraut, I., Rieger, D., Vogel, H., and Vogel, B.: The importance of plume rise on the concentrations and atmospheric impacts of biomass burning aerosol, *Atmospheric Chem. Phys.*, 16, 9201–9219, 2016.
- Wang, W. and Cao, C.: NOAA-20 VIIRS sensor data records geometric and radiometric calibration performance one year in-orbit, *IGARSS 2019-2019 IEEE International Geoscience and Remote Sensing Symposium*, 8485–8488, 2019.
- 935 Winker, D. M., Vaughan, M. A., Omar, A., Hu, Y., Powell, K. A., Liu, Z., Hunt, W. H., and Young, S. A.: Overview of the CALIPSO mission and CALIOP data processing algorithms, *J. Atmospheric Ocean. Technol.*, 26, 2310–2323, 2009.
- Wolfe, R. E., Lin, G., Nishihama, M., Tewari, K. P., Tilton, J. C., and Isaacman, A. R.: Suomi NPP VIIRS prelaunch and on-orbit geometric calibration and characterization, *J. Geophys. Res. Atmospheres*, 118, 11,508-11,521, <https://doi.org/10.1002/jgrd.50873>, 2013.
- 940 Wu, L., Hasekamp, O., van Diedenhoven, B., Cairns, B., Yorks, J. E., and Chowdhary, J.: Passive remote sensing of aerosol layer height using near-UV multiangle polarization measurements, *Geophys. Res. Lett.*, 43, 8783–8790, 2016.
- Xu, X., Wang, J., Wang, Y., Zeng, J., Torres, O., Yang, Y., Marshak, A., Reid, J., and Miller, S.: Passive remote sensing of altitude and optical depth of dust plumes using the oxygen A and B bands: First results from EPIC/DSCOVR at Lagrange-1 point, *Geophys. Res. Lett.*, 44, 7544–7554, 2017.
- 945 Xu, X., Wang, J., Wang, Y., Zeng, J., Torres, O., Reid, J. S., Miller, S. D., Martins, J. V., and Remer, L. A.: Detecting layer height of smoke aerosols over vegetated land and water surfaces via oxygen absorption bands: hourly results from EPIC/DSCOVR in deep space, *Atmospheric Meas. Tech.*, 12, 3269–3288, 2019.